SAND2019-14793J

Pore-scale analysis of calcium carbonate precipitation and dissolution kinetics in a microfluidic device

Hongkyu Yoon[1],*, Kirsten N. Chojnicki[1], and Mario J. Martinez[2]

[1]Geoscience Research and Applications, Sandia National Laboratories, Albuquerque, NM, USA
[2]Fluid and Reactive Processes Department, Engineering Sciences, Sandia National Laboratories, Albuquerque, NM, USA
* Corresponding author

ABSTRACT

In this work we have characterized the calcium carbonate ($CaCO_3$) precipitates over time caused by reaction-driven precipitation and dissolution in a micromodel. Reactive solutions were continuously injected through two separate inlets, resulting in transverse-mixing induced precipitation during the precipitation phase. Subsequently, a dissolution phase was conducted by injecting clean water (pH = 4). The evolution of precipitates was imaged in two- and three-dimensions (2-, 3-D) at selected times using optical and confocal microscopy. With estimated reactive surface area, effective precipitation and dissolution rates can be quantitatively compared to results in the previous works. Our comparison indicates that we can evaluate the spatial and temporal variations of effective reactive areas more mechanistically in the microfluidic system only with the knowledge of local hydrodynamics, polymorphs, and comprehensive image analysis. Our analysis clearly highlights the feedback mechanisms between reactions and hydrodynamics. Pore-scale modeling results during the dissolution phase were used to account for experimental observations of dissolved $CaCO_3$ plumes with dissolution of unstable phase of $CaCO_3$. Mineral precipitation and dissolution induces complex dynamic pore structures, thereby impacting pore-scale fluid dynamics. Pore-scale analysis of the evolution of precipitates can reveal the significance of chemical and pore structural controls on reaction and fluid migration.

INTRODUCTION

Reactive transport processes are critically important to control precipitation and dissolution of minerals relevant to energy-related activities and environmental problems in the subsurface[1, 2]. Reactive transport is often impacted by mineral composition, pore geometry, and environmental conditions. It is now well-recognized that pore-scale physics can significantly impact porosity and permeability relationships[3] and thereby influence model predictive capabilities[4, 5]. Over the past decade pore-scale reactive transport processes have been vigorously investigated to delineate the impact of geochemical reactions on the change of hydrogeological properties (e.g., porosity and permeability) and their feedback on reaction rates[6-8]. In particular, mineral growth and dissolution have been investigated under flowing conditions using various techniques: crystal growth using atomic force microscopy[9-11], precipitation dynamics in microfluidics using optical microscopy[12-14] and in small columns using X-ray computed microtomography[15-18] among many others. This body of work demonstrates the importance of reactive surface area on the predictability of the reactive transport system[19-24].

The fluid-solid interfaces can change due to chemical reactions such as mineral precipitation and dissolution processes, leading to an evolving and heterogeneous pore-network, complex reactive transport, and hydrological and mechanical flow processes. Recent multiscale image analysis combined with dissolution experimental work shows that the knowledge on both pore-accessible mineral surface areas and highly reactive mineral phases are required to match the core flood experimental results[24]. In particular, several recent studies[20, 23-25] emphasize that the effective surface area in contact with reactive fluid is important to properly account for the impact of mineral geometries and local hydrodynamics on the relationship between reactive surface areas and bulk reaction rates. This effective surface area that accounts for actual surface area contributing to fluid-solid reactions needs to be distinguished from geometric and/or specific surface areas commonly used in traditional means of estimating reactive surface area in order to develop reliable models for evolving and heterogeneous pore networks.

For carbonate precipitation, polymorphs of calcium carbonate also influence the reactive surface area and precipitate sizes, thereby impacting reaction rates. In particular, highly super-saturated experimental conditions can lead to the formation of nano-size amorphous calcium carbonate

(ACC) that may attach to the surface of minerals, resulting in successive calcium carbonate crystallization. The transformation of thermodynamically less stable forms of calcium carbonate into more stable crystalline forms has also been investigated over variable timeframes[26-29]. Interfacial reactive processes involving mineral precipitation/dissolution and biogeochemical processes have been studied using pore-scale experimental and modeling efforts with different geochemical compositions[14, 30-32], flow rates[30, 33], and pore configurations[34]. In addition, recent studies highlight the importance of surface roughness at pore and molecular scales on upscaling of reaction rates[20, 25].

The objective of this work is to quantify the change of two- and three-dimensional (2-D and 3-D) reactive surface area over time to evaluate how to estimate precipitation and dissolution reaction rates in a micromodel. Both optical and laser scanning confocal microscopy (LSCM) were used to obtain 2-D and 3-D images of precipitates at different resolutions and image analysis results were used to compare the effective surface area with the geometry-based surface area for evaluating how to define reactive surface area correctly. Dissolved ion transport observed during dissolution phase is compared to results from a 2-D pore-scale reactive transport model to account for the mechanism of dissolution process in the micromodel. Implications of $CaCO_3$ precipitation and dissolution are discussed to highlight the importance of reactive surface area on reactive transport in the subsurface.

MATERIALS and METHODS

Chemicals

Two influent solutions of calcium chloride ($CaCl_2$, >97% Sigma Aldrich) and sodium carbonate (Na_2CO_3, >99.5% Sigma Aldrich) were prepared at a concentration of 10 mM. For all testing nanopure water (Barnstead NANOpure Diamond, 18.2 mΩ/cm) was used. The measured pH values were ~6 and 11 for $CaCl_2$ and Na_2CO_3 solutions during precipitation, respectively, and 4 for water solution (adjusted with HCl) during dissolution.

Micromodel and Experimental Setup

Experiments were conducted in a microfluidic pore network (i.e., micromodel) that was fabricated using standard photolithograph techniques and inductively coupled plasma-deep reactive ion etching (ICP-DRIE) on a silicon wafer. The micromodel fabrication and assembly processes were previously reported in the literature[14, 35]. The micromodel consisted of a homogeneous pore network that is 2-cm long, 1-cm wide, and 10-μm deep (Figure S1). The pore network contains a staggered array of cylindrical posts, 300-μm in diameter, separated by pore bodies and throats with dimensions of 180 μm and 40 μm, respectively (Figure S1). The pore network porosity was ~0.39. The micromodel contains two inlets and one outlet, each with a NanoPort Assembly (IDEX Health Science, N-333). The micromodel was cleaned and saturated with nanopure water prior to the injection of chemicals. For the precipitation phase each solution ($CaCl_2$ and Na_2CO_3) was injected into a separate inlet using a syringe pump (Harvard apparatus, model PHD2000) at a volumetric flow rate of 50 μL/h (Darcy velocity = 1.67 cm/min). All of the solution exited the micromodel through one outlet that was open to the atmosphere and a clean nanopore water solution with a low pH value (pH<2) was flushed into the outlet port at 100 μL/h using a separate tube to prevent clogging by precipitation in the outlet. The precipitation phase continued for 75 hrs, followed by the dissolution phase where nanopure water (pH=4) was injected into both inlets at the same volumetric flow rate (50 μL/h) for ~ 150 hrs.

Microscope Imaging

Mixing between the two reactants resulted in calcium carbonate ($CaCO_3$) precipitation, which was imaged at selected time intervals. Images were acquired with both CCD camera (Axiocam) and laser scanning confocal microscope (Zeiss LSM510). To assess the precipitate behavior, mosaic images were made of a collection of 2-D optical images taken at 1 μm/pixel resolution over the micromodel region with reactions (Figures 1 and S2). Before the mosaic was created, an additional image was taken outside of the pore network and then applied to each image to correct non-uniform illumination. To assess the 3-D precipitate morphology in single pore body, the LSCM was used to acquire a stack of images at 1 μm vertical interval over the micromodel depth (10 μm), following Park et al.[36] and Lima et al.[37]. Images with three different horizontal resolutions (0.63 μm, 0.31 μm and 0.20 μm per pixel) with imaging parameters reported in Table S1 were taken (Fig. S3), but based on preliminary analysis the finest resolution image (0.20 μm) was used to conduct quantitative analysis. Following Boyd et al.[30], Raman spectroscopy was performed to identify the crystal polymorphs which were determined based on the Raman spectra of calcium carbonates in the literature[38]. The detailed description is provided in the section S1.

Image process of $CaCO_3$ Precipitates

All images were segmented to identify precipitates using a threshold value that was adjusted manually for each (mosaic) image due to different intensities in background shading. A combination of different filters (e.g., median, sharp contrast, normalization) was applied based on different features of each image after non-precipitate regions including cylinders were manually masked. In particular, the shadow effect around cylinders due to non-uniform illumination and the non-smooth edges of the cylinders without precipitates were manually removed to improve the image processing as shown in the supplemental information (see Fig. S4 for an example). For a 3-D stack of LSCM images each image was processed independently to construct a segmented 3-D profile of precipitates. A set of image processing filters (e.g., filling holes, erode, dilate) was applied to produce segmented images within ± ~5 % reproducibility.

$CaCO_3$ Reaction Rates and Reactive Surface Area

For segmented 2-D images in multiple pores at three different locations (upstream, midstream, and downstream in Figure 1) the number of pixels containing $CaCO_3$ precipitate was counted to compute the overall reaction rates (mol/s) as $[A_{2D} \times 10\mu\text{m}/V_{\text{mol}}/\text{dt}]$. A_{2D} is the 2-D horizontal area of the precipitate [the number of pixels × area of each pixel ($=1\ \mu\text{m}^2$)], 10µm is the micromodel depth, V_{mol} is a molar volume of calcite ($36.94\ \text{cm}^3/\text{mol}$), and dt is the time interval of each image from the previous time step. It is assumed that the 2-D area of the precipitate based on 2-D images is uniform over the micromodel depth. In addition the perimeter of precipitates was counted using an analyze particles plug-in in ImageJ/Fiji[39] to compute the effective reaction rates ($\text{mol/m}^2\text{/s}$) as $[(A_{2D} \times 10\mu\text{m}/V_{\text{mol}}/\text{dt})/RSA_{2D\_avg}]$. The term in the parenthesis is the overall reaction rate ((mol/s), RSA_{2D_avg} is the average of 2-D vertical reactive surface area of the precipitate between the previous and current times computed as [the number of perimeter pixels × pixel resolution (µm) ×10µm] where 10µm is the micromodel depth. For single pore LSCM images the 3-D reactive surface area (RSA_{3D}) and volume (V_{3D}) for precipitates were computed using a 3-D objects counter plug-in in Fiji[40]. A stack of segmented 3-D images was directly used for analysis, while a 2-D image was used to compute the volume (V_{2D}) with the uniform vertical profile. It is noted that the reactive surface of precipitates in a single pore is dominantly vertical because top and bottom faces of the precipitates are confined by the micromodel. Although a micromodel is typically considered a 2-D system due to its shallow depth, we evaluated 2-D and 3-D reactive surface areas in single pores to account for the impact of the vertical dimension and image resolution on the reactive surface area.

Pore Scale Reactive Transport

A 2-D pore-scale reactive transport model[2, 13, 30] was modified to simulate the distribution of pH, flow velocity, species concentrations at a specific time during the dissolution phase under the experimental conditions in this study. Briefly, an open source lattice Boltzmann library[41] was used to solve for fluid velocity fields in pore spaces and a finite volume method was used to solve for reactive transport including homogeneous and heterogeneous reactions. For the micromodel with precipitates, the model domain was 3.78 mm x 2.89 mm with an empty inlet region (0.15 mm) and a 1 μm grid spacing was used to reflect the 2-D image resolution. The clean water (pH=4.0) was uniformly injected through both inlets. The primary species consists of H^+, HCO_3^-, and Ca^{2+}, and the secondary species concentrations were computed through the mass action law. The overall reaction rate of $CaCO_3$ precipitation and dissolution (R_m, mol/s) has the form:

$$R_m = S_r I_m = -S_r k_r \left(1 - \frac{a_{Ca^{2+}} a_{CO_3{}^{2-}}}{K_{sp}}\right) \qquad (1)$$

where S_r is the reactive surface area of precipitation and dissolution, I_m is the effective reaction rate (mol/m^2/s), k_r $\left(= k_1 a_{H^+} + k_2 a_{H_2CO_3} + k_3\right)$ is the overall kinetic rate constant with k_1 (8.9×10^{-1}), k_2 (5.01×10^{-4}), and k_3 (6.6×10^{-7}) (mol/m^2/s)[42], a_i is the activity of species i, and K_{sp} is the solubility product of $CaCO_3$. Here, we define the supersaturation ratio (SR) as the ratio of ion activity product ($a_{Ca^{2+}} a_{CO_3{}^{2-}}$) to K_{sp}. To evaluate the effect of reactive surface area and polymorph of $CaCO_3$ precipitate on reaction rates in equation (1), two different reactive surface area values (S_r) based on image analysis and stability of precipitates and two different solubility products (K_{sp} for calcite and aragonite) were used in pore scale simulations. The description of the cases is presented in the results of pore scale simulations.

RESULTS and DISCUSSION

$CaCO_3$ Precipitation in Multiple Pores

Images of $CaCO_3$ precipitates in multiple pores are shown for both precipitation and dissolution phases in Figure 1c (see Figure S5 for high resolution images). As two solutions were injected separately, transverse mixing between calcium and carbonate ions created a reaction zone where $CaCO_3$ precipitates formed within pore bodies and around the cylindrical posts. Near the inlet, precipitates formed at the mixing line in the micromodel and extended less than a single pore body in the transverse direction, while the precipitates formed across 3 pore bodies surrounding the primary mixing line downstream. Early precipitation processes in the micromodel system typically involve homogeneous nucleation, particle attachment, and crystal growth, which has been investigated in the previous works[13, 30]. During the precipitation phase, more precipitates in the midstream and downstream locations were observed than in the upstream location. This is likely due to combination of precipitates-induced spreading of reactant plume and enhanced mixing across the interface of two reactant plumes[13, 34]. Spreading due to heterogeneous pore structure such as one caused by precipitates leads to the stretching of interfaces of the reactant plume, while mixing across the reactive interfaces is governed by local hydrodynamic dispersion[43-45].

Both precipitation patterns and the amount of precipitates over time are evaluated to compare the current results with previous studies in micromodels[14, 30] where solute concentrations and micromodel geometries were similar. Overall precipitation patterns in terms of precipitate spreading and various shapes of precipitants within a few transverse pore bodies in 2-D images are similar to previous $CaCO_3$ precipitation studies[14, 30]. The similarity in precipitate patterns over a range of micromodel depths (10 μm with a Darcy velocity of 1.67 cm/min in this study .vs. 20 μm (1.25 cm/min)[14], and 35 μm (0.92 cm/min)[30]) suggests that the vertical gradient or advective component of the reactive ion concentrations can be negligible at the low Reynolds numbers (<<1, i.e., laminar flow) and a diffusion time scale over the micromodel depth in this study is much smaller than a retention time scale in each pore block. Hence, the difference in the steady state times among these studies is likely controlled by the flux of reactive species when the overall pattern of the pore network and solution chemistry are similar. Quantitative comparison of this work with the previous works will be performed in the section of reaction rates.

During the precipitation phase, the precipitate area (A_{2D}) generally increased downstream due to the increase of transverse mixing with the travel distance (Figure 2 and Table S2). The change of A_{2D} in up-, mid-, and down-stream regions reveals that precipitation rapidly occurred for the first 3.1 hr in all regions, and then was followed by slow dissolution in the upstream region, slowed down with a continuous growth until ~56 hr (followed by slow dissolution) in the midstream region, and continuously occurred to the end of precipitation phase in the downstream region. The slightly non-monotonic behavior in the upstream can be attributed to a higher concentration of reactive products, resulting in fast precipitation leading to a rapid decrease in transverse mixing. Figure 1c clearly shows the formation of distinct crystal phases between 1.8 and 3.1 hrs in the upstream region, resulting in the change of local hydrodynamics (see Figure S5 for high resolution image). In addition, the upper mixing stream in the midstream region at 1.8 hr almost moved upward to form a new precipitation line at 3.1 hr, while relatively big crystals (all of calcite) remained. As demonstrated by previous pore-scale modeling[13], this change can result from the pore blocking of precipitates upstream, so the transverse mixing in the midstream region is influenced. The comparison of vertical surface area (*RSA*) with precipitate (horizontal) area (A_{2D}) from 3.1 hr to 75 hr in Figure 2 shows that A_{2D} tends to slightly decrease upstream, increase and then decrease midstream, and largely increase downstream. *RSA* also followed the trend of A_{2D} change, but the rate of change of *RSA* (i.e., slope in Figure 2) was higher than that of A_{2D}, implying that smaller precipitates decrease more rapidly upstream (e.g., location B in Figure S6 and Figure S10), but new precipitates form downstream to increase both A_{2D} and *RSA* (Figures 1 and S7).

$CaCO_3$ Dissolution in Multiple Pores

Following the precipitation phase, the dissolution phase was examined. Most notably, dissolved $CaCO_3$ were observed as dark aqueous phase plumes in the upper side of the micromodel (Figure 1b-c). Near the inlet, the plumes of dissolved precipitate formed in direct contact with precipitates. However, further downstream the plumes appeared in pores without precipitates that were 2 to 3 pore bodies away from pores with precipitates. As the dissolution continued, $CaCO_3$

crystals along the central precipitate line completely dissolved, and the plumes were observed from both sides of the micromodel (e.g., 89 hr of dissolution). During dissolution, the amount of precipitate areas decreased by ~73-98% over ~142 hrs (Figure 2 & Table S2). The observation of the dissolved plumes will be further discussed in the pore-scale simulation results.

For dissolution at 24 hr (t=99 hr in Figure 2), precipitate area (A_{2D}) changed differently in three regions where A_{2D} decreased by ~23% in the upstream, and slightly increased by 2.4 ~ 4.3% in the midstream and downstream. The change of reactive surface area (*RSA*) shows that *RSA* in the upstream decreased by ~16%, did not change in the midstream, and increased by 11.1% downstream over 24 hrs of dissolution (Table S2). The different trend between upstream and downstream can be explained by correlation between local reactions and hydrodynamics where dissolved ions in both upper and lower sides of the central precipitate line in the upstream can produce reactant ions (i.e., HCO_3^- and Ca^{2+}), resulting in precipitation in the midstream. Then undersaturated solution in the downstream due to reaction in the midstream may contribute to the dissolution as well as precipitation indicated by the increase of *RSA*. The increase of *RSA* in downstream can be explained by the growth of small precipitates that can contribute to the *RSA* increase higher than A_{2D} change (see Figure S7). For example, a radius of 5 μm precipitate can contribute to the *RSA* increase four times higher than A_{2D} with a conservative assumption of vertically uniform precipitate profile in depth of the micromodel (5 μm). The impact of local hydrodynamics on the reaction patterns will be discussed in the pore scale simulation results. Most of the crystals remained at 89 hr were calcite that was slowly dissolved compared to other polymorphs (aragonite and ACC) as shown in Raman analysis (Figure S8). The dissolved plume in the entire upstream region at 89 hr (Figure 1) indicates that all precipitates have been exposed to fluid flowing (i.e., no vertical pore blocking).

$CaCO_3$ Precipitation and Dissolution in Single Pore

To explore how local variations in flow and transport may influence the precipitation patterns and polymorphs, representative patterns of precipitates were examined in five single pore locations at different times (Figure 3), and the amount of precipitates and reactive surface areas at two locations (*i* & *v*) were also evaluated. All images were taken along the central mixing line (Figure 1) where precipitation was confined to and continuous along the central mixing line (location *i*@6 hr), discrete large and small crystals formed (*ii*@6 hr), and individual large crystal(s) and continuous precipitates formed (*iii*@6 hr and *iv*-*v*@28 hr). While some large crystals formed in isolation of the mixing line (location *iv*), others attached to the mixing line (*v*), possibly due to the initial nucleation or crystal growth locations downstream. Raman spectra analysis performed during the dissolution phase indicate that the thin continuous precipitate line in the first pore body (location *i*) could consist of ACC and aragonite, distinctive rhombohedral shape is calcite, smooth curved boundary shape is predominantly aragonite, and aggregates of smaller particles are mostly aragonite, but sometimes include calcite (see more examples in Figure S8).

In individual pores, the dissolution behavior depends strongly on the local precipitate pattern and $CaCO_3$ crystal phase. For the continuous precipitate line near the inlet (*i*@94 hr), a single breach in the thin precipitate line occurred along with the dissolved precipitate plume after irregular surfaces of aragonite precipitates were dissolved (e.g., upstream image at 24 hr during the dissolution phase in Figure 1c). After the breach, flow was likely to bypass the remaining part of the precipitate, resulting in a relatively slow dissolution of thin ACC. For the cases without a continuous precipitate line (e.g., *ii*@94 hrs) discrete precipitates including two big aragonite crystals dissolved relatively fast due to a higher solubility and possibly meta-stable phase of aragonite. As a result, a large reactive surface area of small precipitates can be dissolved fast once flow was allowed through the pore body as shown in the image after 24 hrs during the dissolution phase (e.g., Figure S1 for high resolution image). For a continuous precipitate line and various sizes and polymorphs of precipitates (locations *iii*-*v*), most of the small precipitates were dissolved faster than a big calcite crystal (location *v*), while the dissolution of continuous precipitate lines was affected by $CaCO_3$ polymorph (aragonite in location *iv* and mix of aragonite and calcite in locations *iii* and *v*) and local hydrodynamics and solution chemistry. Overall, the evolution and extent of dissolution depends on the initial state of the pore geometry as well as the local and global evolution in the hydrodynamics as dissolution proceeds.

Impact of Image Resolution on Quantitative Analysis

The precipitate area (A_{2D}) and perimeter of precipitates as the reactive surface area (*RSA*) in the first pore body (location *i* in Figure 3) were estimated using 2-D images taken at four different resolutions of 0.2, 0.63, 0.31, and 1 μm per pixel during both precipitation phase (t=55hr) and dissolution phase (t=94 hr) (Figure 4 and Figure S9 for high resolution images). Comparison of A_{2D} and *RSA* analysis (Figure 4) shows that the accuracy of the analysis decreases with decreasing the image resolution. In particular, the estimates at 1 μm resolution become lower than those at 0.2 μm resolution significantly. This discrepancy is primarily due to clear image quality at 0.2 and 0.31 μm resolutions compared to slightly blurred image of precipitates with slightly thicker shade around the cylinder at 0.63 and 1 μm resolutions (Figure S9). This comparison clearly highlights the importance of image resolution and quality on the estimation of reaction rates and *RSA* and previous analysis based on the relatively coarse resolution optical images (~2 μm[14, 30] and ~3 μm[17] resolution) would provide qualitative trends instead of accurate quantitative results. To improve the quantitative analysis of 1 μm resolution images, upscaled segmented images from 1 μm to 0.2 μm resolution using bicubic interpolation resulted in increasing the accuracy of precipitate area (A_{2D}) significantly and the perimeter of precipitate (*RSA*) slightly (Figure 4). For all quantitative analysis in this study, we used images at 0.2 μm resolution for the volume and *RSA* of precipitates in single pore and the upscaled segmented image from 1 to 0.2 μm resolution using bicubic interpolation in multiple pores.

3-D Estimate of $CaCO_3$ Reactive Surface Area in Single Pore Images

2-D and 3-D images at 0.2 μm resolution in locations *i* & *v* were analyzed to estimate the reactive surface area (RSA_{2D}, RSA_{3D}) and volume (V_{2D}, V_{3D}) of precipitates at four different times. 2-D images in two locations (*i* & *v*) are shown in Figure 3 and a 3-D vertical profile in location *i* is shown in Figure S10. In addition, confocal images taken at the bottom, center, and top of the micromodel in two locations (*ii* & *v*) are shown in Figures S11-S12. RSA_{3D} was higher than RSA_{2D} by a factor of ~1.73 (ranging from 1.59 to 1.92) and 1.06 (ranging from 1.02 to 1.08) in locations *i* & *v*, respectively, while V_{2D} and V_{3D} were relatively similar at both locations. The range of the RSA_{3D}/RSA_{2D} ratio was within the theoretical surface roughness factor (1-6.13 with most of them within 2.5) for various rough fracture surface types[20]. The similarity of volume estimates can attribute to the similarity between 2-D and projected 3-D images (Figure S10) where the boundary of 2-D image at location *i* matches the average of 3-D segmented image relatively well. Hence, the high resolution 2-D image can be used to estimate the volume or area of precipitates. The higher RSA_{3D} compared to RSA_{2D} at location *i* is mainly due to the change of vertical surface roughness as shown in Figure S10. The similarity of RSA_{3D} to RSA_{2D} at location *v* was mainly due to the presence of a big calcite crystal and a smooth vertical surface of precipitate line. Crystals tend to grow slowly downstream and a stable form of calcite grows as shown in Figure 3 (location *v*). It should be noted that as in location *i* where a higher geometrical surface area does not result in a fast dissolution, the overall reaction rate is also strongly affected by local hydrodynamics and solution chemistry[20, 24].

$CaCO_3$ Reaction Rates

Although the initial pattern of pore structure was homogeneous, precipitation increased the complexity of pore structures, resulting in a heterogeneous pore structure with different reactive surfaces. In previous microfluidic works[14, 30] our new calculation show that overall precipitation rates were estimated to be $0.5\sim4\times10^{-11}$ and $3\sim4\times10^{-11}$ mol/s over the whole micromodel area[14] and a third of the whole micromodel length[30], respectively. A similar range of precipitation rates even with different analysis areas was mainly due to different precipitation patterns used for analysis, wherein experimental results with only one dominant precipitation line and multiple precipitation lines were analyzed in Zhang et al. [14] and in Boyd et al. [30], respectively. This different precipitation patterns in the micromodel system can be caused by a couple of factors including local fluctuation of streamline due to the micromodel movement during imaging, mechanical vibration of pumping system, and the change of local hydrodynamics along the centerline of micromodel due to precipitates. For the first 3.1 hr the sum of reaction rates in upstream and midstream regions was calculated as $3 \sim 5\times10^{-12}$ mol/s (Table 1) which is comparable with the value in Boyd et al.[30] by considering the micromodel depth (10 vs. 35 μm) and flow rates (100 vs. 192 μL/hr). Since these two previous micromodel studies did not compute an effective reactive area, it is not possible to compare these works to other systems. Here, we demonstrate the significance of realistic reactive surface area on the estimation of reaction rates in the microfluidic work.

With the vertical *RSA* the estimated precipitation rates (I_m in Eq. (1), mol/m^2/s) were $1.4–3.0 \times 10^{-5}$ at 1.8 hr, $8.5–19 \times 10^{-6}$ at 3.1 hr, and then $0.9–6.4 \times 10^{-7}$ until 75 hr except net dissolution rates upstream and midstream (Table 1). The overall kinetic rate constant (k_r) in Eq. (1) has a range of ~6.6×10^{-7}–5×10^{-6} mol/m^2/s with the literature constant values (k_1, k_2, k_3) (e.g., Chou et al. [42]) given the experimental conditions (pH = 6–11, total carbonate concentration = 2×10^{-5} – 0.01 M) in this work. A supersaturation ratio (SR=IAP/ K_{sp}) in Eq. (1) was calculated up to ~ 400 and ~ 2.6 for calcite and ACC, respectively, at the beginning of precipitation phase along the central mixing line using the pore scale simulation[30]. Thus, the higher precipitation rates at early times (e.g., 1.4–3.0 × 10^{-5} mol/m^2/s at 1.8 hr) based on image analysis in this work can be comparable with the product (~ an order of 10^{-5}) of k_r and (1-SR) based on the literature value and experimental conditions during the beginning of precipitation phase. This indicates that if ion concentrations in the active reaction region (i.e., primary precipitation line in this work) can be accurately estimated at early times before significant pore blocking, the estimation of *RSA* at 1.8 hr can be considered realistic reactive surface area when the geometrically estimated surface area are predominantly in contact with reactive fluid.

The effective precipitation rates decreased more significantly upstream and slightly downstream at 3.1 hr, compared to those at 1.8 hr (Table 1), reflecting that the change of local hydrodynamics due to precipitates upstream caused pore blocking along the precipitation line (i.e., no transverse mixing). As a result, the effective reaction rates (I_m in Eq. (1)) decreased more upstream than midstream and downstream over time (Table 1). Comparison of *RSA* and I_m at 3.1 hr and 75 hr shows that the RSA values were within ±24 %, but the I_m value at the downstream region was lower by approximately two orders of magnitude at 75 hr than at 3.1 hr and even negative (i.e., overall dissolution dominant reaction) at the upstream earlier (after 3.1 hr) and midstream later (after 56.2 hr). This clearly demonstrates that the effective surface area based on the geometrical estimation is not the actual reactive surface area in contact with reactive fluid. Instead, only a fraction of sites on the surface is reactive, which would explain slower rate estimation of I_m and R_m in this work. This is also related to the impact of local hydrodynamics on reactions. The bulk flow can bypass the highly precipitate region where dissolution and reprecipitation can occur as in the Oswalt ripening process. In this regime, a major limiting step would be transport-limited rather than kinetic-limited.

With the vertical *RSA* dissolution rates at t= 24 hr during the dissolution phase were 22.7, –2.9, and -6.8×10^{-8} mol/m^2/s from upstream to downstream (Table 1, Figures 1c and S5 for microscopic images). As discussed previously, the dissolution rates indicated that dissolved species upstream reprecipitated midstream and downstream (e.g., Figure S7). Here we limit our discussion to the upstream dissolution rate where we can reasonably assume that dissolution is predominant. The dissolution rate of 2.27×10^{-7} mol/m^2/s was higher by an order of magnitude than the value obtained in other calcite dissolution works (e.g., Molins et al.[21]; Pokrovsky et al.[46]). In the previous work[21] the discrepancy among column, batch, and simulation results was explained by a couple of factors including different sources of calcite crystals, rate-limiting steps, and kinetic rate models. In this work, the estimated RSA at 24 hr during dissolution phase can represent pore-accessible mineral surface areas well since undersaturated inlet solution can flow through most of precipitates. Hence, the discrepancy can be attributed to the presence of $CaCO_3$ polymorphs at the beginning of dissolution phase that became unstable rapidly, resulting in a fast dissolution rate. This was highlighted in the image of single pore location *ii* (Figure 3) where precipitates were aragonite, and once local hydrodynamics swept through the pore body, all major precipitates were dissolved relatively rapidly. This observation highlights the importance of the knowledge on highly reactive mineral phases similar to the previous work[19, 24] where both pore-accessible mineral surface areas and highly reactive mineral phases were required to match the core flood dissolution experimental results.

For individual pores, spatial and temporal variations can be seen more clearly depending on position and the time (Figure 3). Although the overall precipitate area in location *i* near the inlet did not change much between 6 hr and 55 hr, the vertical surface area decreased by ~ 21 %, indicating that the local reaction is dissolution-dominant after pore blocking. During the dissolution phase, the dissolution rate in the location *i* was 1.1×10^{-11} mol/m^2/s at 94 hr after dissolution which was much lower than the dissolution rate of 4.6×10^{-7} mol/m^2/s at 89 hr in the upstream multiple pore region. This indicates that dissolution occurs very locally where flow can pass through easily. The locality of reactions can be seen in other locations. For example, most of the precipitates in locations *ii*-*iv* were dissolved at 94 hr during the dissolution phase, while a big crystal in location *v* grew, resulting in a net precipitation with a rate of 1.2×10^{-11} mol/m^2/s at 94 hr. Precipitation in location *v* is mainly due to reprecipitation downstream of dissolved species transported from the upper stream regions. This analysis clearly highlights the feedback mechanism between reactions and hydrodynamics.

Pore-scale Reactive Transport Simulation Results

Simulation results of the distribution of pH, flow velocity field, and super-saturation ratio (SR) with respect to calcite are shown in Figure 5. Simulations were performed to obtain the spatial distribution of quantities due to the kinetic reaction in Eq. (1) without updating mineral contents. An experimental image of precipitate distribution at 24 hr during the dissolution phase is also shown. The volumetric fraction of precipitates in the experimental image is assumed to be a unity (i.e., a grid block completely occupied by precipitates) and dissolution reactions are assumed to occur only at the vertical surface of existing precipitates. To account for the effect of surface roughness and different polymorphs on dissolution rate, we performed sensitivity analysis with different reactive vertical surface areas by employing a multiplier of 2 and 100 with the solubility product of calcite (cases 1 and 2) and a multiplier of 100 with the solubility product of aragonite (case 3). The multiplier of 2 represents the increase of vertical surface area based on 3-D profile of precipitates upstream (e.g., location *v*), while the multiplier of 100 would represent the instability of precipitates during the dissolution phase, which was required to match experimental observations in a similar system in Yoon et al.[13]. In particular, we used three cases to evaluate what mechanistic processes may contribute to the formation of dissolved plume above the central precipitate line.

Comparison of the experimental image and velocity and pH distributions shows that dissolved $CaCO_3$ particles transport was constrained with the flow line above the precipitation zones and along the transition zone of pH values from 7 to ~8. This also shows that the dissolved ions diffuse away from the mineral surface and then form dark plumes within thermodynamically favorable pH zone. The newly formed dissolved plume transported along the streamlines slightly away from the precipitate surface and guided by pH values. Comparison of SR (i.e., dissolved ion products) distribution in cases 1 and 2 shows that SR values in case 2 are much higher over larger areas than in case 1, however, both these cases (Figure 5d-e) did not show any significant dissolved ion concentrations above the precipitation line. Instead SR distribution in case 3 with aragonite solubility product and a high multiplier of 100 demonstrates that SR values are higher than cases 1 & 2 and mimic the observed dissolved plume above the precipitate zones (light blue in Figure 5f), demonstrating that both $CaCO_3$ phase and reactivity expressed as the multiplier of 100 are key factors to reproduce the experimental observation.

Cases 1-2 clearly show non-reactive regions below the precipitate line due to no contact between flowing fluid and minerals and these non-reactive regions are much smaller in Case 3 due to higher diffusion of higher dissolved concentrations driven by higher reaction rates. This clearly indicates that geometrically estimated reactive surface area can misrepresent actual reactive area without the knowledge of local hydrodynamics[23, 24]. It is also noted that the diffusion dominant region between the central precipitate line and centerline of the micromodel did not show dissolved plume clearly in Figure 1a. This can be explained by the fact that dissolved ions in these regions would tend to move toward favorable precipitate surfaces instead of flow through the streamlines which is shown in the first few pore bodies along the center of the micromodel. In this work the experimental observation highlights that the dissolved plume acts as reactive tracer showing the coupled effect of reactive transport with hydrodynamics.

IMPLICATIONS

Ultimately, the evolution of $CaCO_3$ precipitate patterns in the whole micromodel is significantly influenced by the local variations in precipitation and dissolution. Spatially and temporally averaged reaction rates are likely to be poor estimators of the local reaction rates early during precipitation and late during dissolution. At such times, the flow complexity may be high, inducing the formation of rough mineral surfaces and 3-D effects on the evolution of reactive flow and transport. 2-D expressions for reaction rate that are commonly found in many pore-scale models may oversimplify the reactivity during these complex flow situations and be poor-estimators of their behavior. Recent pore scale reactive transport works[8] including this work demonstrate that pore-scale analysis of evolving precipitates' patterns can reveal (1) the significance of structural and chemical control of fluid migration and cementation and (2) permeability and porosity relationships for various flow and reaction regimes.

Recent multiscale image analysis combined with dissolution experimental work shows that the knowledge on both pore-accessible mineral surface areas and highly reactive mineral phases are required to match the core flood experimental results[24]. In particular, several recent studies[23-25] emphasize that the effective surface area in contact with reactive fluid is important to properly account for the impact of mineral geometries and local hydrodynamics on the relationship between reactive surface areas and bulk reaction rates. Although our work used a clean micromodel with the formation of ACC which posed a problem to quantitatively estimate the precipitation rate at early times, the microfluidic device with controlled mineral surfaces (e.g., calcite chip) would overcome this limitation to study an effective reaction rate in a controlled hydrodynamic system.

Acknowledgments

This work was supported as part of the Center for Frontiers of Subsurface Energy Security, an Energy Frontier Research Center funded by the U.S. Department of Energy, Office of Science, Office of Basic Energy Sciences under Award Number DE-SC0001114. We thank Prof. Charles J. Werth for providing the micromodel and Dr. Kyle Michelson for Raman analysis. This paper describes objective technical results and analysis. Any subjective views or opinions that might be expressed in the paper do not necessarily represent the views of the U.S. Department of Energy or the United States Government. Sandia National Laboratories is a multimission laboratory managed and operated by National Technology and Engineering Solutions of Sandia, LLC., a wholly owned subsidiary of Honeywell International, Inc., for the U.S. Department of Energy's National Nuclear Security Administration under contract DE-NA-0003525.

Supporting Information

There are supplemental figures for high resolution images and tables for additional image analysis.

Literature Cited

1. Li, L.; Maher, K.; Navarre-Sitchler, A.; Druhan, J.; Meile, C.; Lawrence, C.; Moore, J.; Perdrial, J.; Sullivan, P.; Thompson, A., Expanding the role of reactive transport models in critical zone processes. *Earth-Science Reviews* **2017,** *165*, 280-301.
2. Yoon, H.; Kang, Q.; Valocchi, A. J., Lattice Boltzmann-based approaches for pore-scale reactive transport. *Reviews in mineralogy geochemistry* **2015,** *80*, 393-431.
3. Steefel, C. I.; Emmanuel, S.; Anovitz, L. M., *Pore-scale geochemical processes*. Mineralogical Society of America: 2015.
4. Altman, S. J.; Aminzadeh, B.; Balhoff, M. T.; Bennett, P. C.; Bryant, S. L.; Cardenas, M. B.; Chaudhary, K.; Cygan, R. T.; Deng, W.; Dewers, T., Chemical and hydrodynamic mechanisms for long-term geological carbon storage. *The Journal of Physical Chemistry C* **2014,** *118*, (28), 15103-15113.
5. Steefel, C.; Appelo, C.; Arora, B.; Jacques, D.; Kalbacher, T.; Kolditz, O.; Lagneau, V.; Lichtner, P.; Mayer, K. U.; Meeussen, J., Reactive transport codes for subsurface environmental simulation. *Computational Geosciences* **2015,** *19*, (3), 445-478.
6. Soulaine, C.; Roman, S.; Kovscek, A.; Tchelepi, H. A., Mineral dissolution and wormholing from a pore-scale perspective. *Journal of Fluid Mechanics* **2017,** *827*, 457-483.
7. Szymczak, P.; Ladd, A. J., Reactive-infiltration instabilities in rocks. Fracture dissolution. *Journal of Fluid Mechanics* **2012,** *702*, 239-264.
8. Yoon, H.; Major, J.; Dewers, T.; Eichhubl, P., Application of a pore-scale reactive transport model to a natural analog for reaction-induced pore alterations. *Journal of Petroleum Science Engineering* **2017,** *155*, 11-20.
9. De Yoreo, J. J.; Vekilov, P., Principles of crystal nucleation and growth. *Reviews in mineralogy geochemistry* **2003,** *54*, 57-93.
10. Stack, A. G.; Grantham, M. C., Growth rate of calcite steps as a function of aqueous calcium-to-carbonate ratio: independent attachment and detachment of calcium and carbonate ions. *J Crystal Growth* **2010,** *10*, (3), 1409-1413.
11. Teng, H. H.; Dove, P. M.; De Yoreo, J. J., Kinetics of calcite growth: surface processes and relationships to macroscopic rate laws. *Geochimica et Cosmochimica Acta* **2000,** *64*, (13), 2255-2266.
12. Singh, R.; Yoon, H.; Sanford, R. A.; Katz, L.; Fouke, B. W.; Werth, C. J., Metabolism-induced CaCO3 biomineralization during reactive transport in a micromodel: Implications for porosity alteration. *Environmental science & technology* **2015,** *49*, (20), 12094-12104.
13. Yoon, H.; Valocchi, A. J.; Werth, C. J.; Dewers, T., Pore-scale simulation of mixing-induced calcium carbonate precipitation and dissolution in a microfluidic pore network. *Water Resources Research* **2012,** *48*, (2).
14. Zhang, C.; Dehoff, K.; Hess, N.; Oostrom, M.; Wietsma, T. W.; Valocchi, A. J.; Fouke, B. W.; Werth, C. J., Pore-scale study of transverse mixing induced CaCO3 precipitation and permeability reduction in a model subsurface sedimentary system. *Environmental science & technology* **2010,** *44*, (20), 7833-7838.
15. Gouze, P.; Noiriel, C.; Bruderer, C.; Loggia, D.; Leprovost, R., X-ray tomography characterization of fracture surfaces during dissolution. *Geophysical Research Letters* **2003,** *30*, (5).

16. Noiriel, C.; Gouze, P.; Bernard, D., Investigation of porosity and permeability effects from microstructure changes during limestone dissolution. *Geophysical research letters* **2004,** *31*, (24).

17. Noiriel, C.; Steefel, C. I.; Yang, L.; Bernard, D., Effects of pore-scale precipitation on permeability and flow. *Advances in water resources* **2016,** *95*, 125-137.

18. Gao, J.; Xing, H.; Tian, Z.; Pearce, J. K.; Sedek, M.; Golding, S. D.; Rudolph, V., Reactive transport in porous media for CO2 sequestration: Pore scale modeling using the lattice Boltzmann method. *Computers & Geosciences* **2017,** *98*, 9-20.

19. Beckingham, L. E.; Mitnick, E. H.; Steefel, C. I.; Zhang, S.; Voltolini, M.; Swift, A. M.; Yang, L.; Cole, D. R.; Sheets, J. M.; Ajo-Franklin, J. B., Evaluation of mineral reactive surface area estimates for prediction of reactivity of a multi-mineral sediment. *Geochimica et Cosmochimica Acta* **2016,** *188*, 310-329.

20. Deng, H.; Molins, S.; Trebotich, D.; Steefel, C.; DePaolo, D., Pore-scale numerical investigation of the impacts of surface roughness: Upscaling of reaction rates in rough fractures. *Geochimica et Cosmochimica Acta* **2018,** *239*, 374-389.

21. Molins, S.; Trebotich, D.; Yang, L.; Ajo-Franklin, J. B.; Ligocki, T. J.; Shen, C.; Steefel, C. I.; technology, Pore-scale controls on calcite dissolution rates from flow-through laboratory and numerical experiments. *Environmental science & technology* **2014,** *48*, (13), 7453-7460.

22. Wen, H.; Li, L., An upscaled rate law for mineral dissolution in heterogeneous media: The role of time and length scales. *Geochimica et Cosmochimica Acta* **2018,** *235*, 1-20.

23. Salehikhoo, F.; Li, L., The role of magnesite spatial distribution patterns in determining dissolution rates: When do they matter? *Geochimica et Cosmochimica Acta* **2015,** *155*, 107-121.

24. Beckingham, L. E.; Steefel, C. I.; Swift, A. M.; Voltolini, M.; Yang, L.; Anovitz, L. M.; Sheets, J. M.; Cole, D. R.; Kneafsey, T. J.; Mitnick, E. H., Evaluation of accessible mineral surface areas for improved prediction of mineral reaction rates in porous media. *Geochimica et Cosmochimica Acta* **2017,** *205*, 31-49.

25. de Assis, T. A.; Reis, F. D. A. A., Dissolution of minerals with rough surfaces. *Geochimica et Cosmochimica Acta* **2018,** *228*, 27-41.

26. Liu, J.; Pancera, S.; Boyko, V.; Shukla, A.; Narayanan, T.; Huber, K., Evaluation of the particle growth of amorphous calcium carbonate in water by means of the porod invariant from SAXS. *Langmuir* **2010,** *26*, (22), 17405-17412.

27. Ogino, T.; Suzuki, T.; Sawada, K., The formation and transformation mechanism of calcium carbonate in water. *Geochimica et Cosmochimica Acta* **1987,** *51*, (10), 2757-2767.

28. Pouget, E. M.; Bomans, P. H. H.; Goos, J. A. C. M.; Frederik, P. M.; Sommerdijk, N. A. J. M., The initial stages of template-controlled CaCO3 formation revealed by cryo-TEM. *Science* **2009,** *323*, (5920), 1455-1458.

29. Rieger, J.; Frechen, T.; Cox, G.; Heckmann, W.; Schmidt, C.; Thieme, J., Precursor structures in the crystallization/precipitation processes of CaCO 3 and control of particle formation by polyelectrolytes. *Faraday discussions* **2007,** *136*, 265-277.

30. Boyd, V.; Yoon, H.; Zhang, C.; Oostrom, M.; Hess, N.; Fouke, B.; Valocchi, A. J.; Werth, C., Influence of Mg2+ on CaCO3 precipitation during subsurface reactive transport in a homogeneous silicon-etched pore network. *Geochimica et Cosmochimica Acta* **2014,** *135*, 321-335.

31. Fanizza, M. F.; Yoon, H.; Zhang, C.; Oostrom, M.; Wietsma, T. W.; Hess, N. J.; Bowden, M. E.; Strathmann, T. J.; Finneran, K. T.; Werth, C. J., Pore-scale evaluation of uranyl

phosphate precipitation in a model groundwater system. *Water Resources Research* **2013,** *49*, (2), 874-890.

32. Yoon, H.; Leibeling, S.; Zhang, C.; Müller, R. H.; Werth, C. J.; Zilles, J. L., Adaptation of Delftia acidovorans for degradation of 2, 4-dichlorophenoxyacetate in a microfluidic porous medium. *Biodegradation* **2014,** *25*, (4), 595-604.

33. Tartakovsky, A. M.; Redden, G.; Lichtner, P. C.; Scheibe, T. D.; Meakin, P., Mixing-induced precipitation: Experimental study and multiscale numerical analysis. *Water Resources Research* **2008,** *44*, (6).

34. Willingham, T. W.; Werth, C. J.; Valocchi, A. J., Evaluation of the effects of porous media structure on mixing-controlled reactions using pore-scale modeling and micromodel experiments. *Environmental science & technology* **2008,** *42*, (9), 3185-3193.

35. Chomsurin, C.; Werth, C. J., Analysis of pore-scale nonaqueous phase liquid dissolution in etched silicon pore networks. *Water resources research* **2003,** *39*, (9).

36. Park, J. S.; Choi, C. K.; Kihm, K. D., Optically sliced micro-PIV using confocal laser scanning microscopy (CLSM). *Experiments in Fluids* **2004,** *37*, (1), 105-119.

37. Lima, R.; Wada, S.; Tsubota, K.-i.; Yamaguchi, T., Confocal micro-PIV measurements of three-dimensional profiles of cell suspension flow in a square microchannel. *Measurement Science and Technology* **2006,** *17*, (4), 797.

38. Nehrke, G.; Poigner, H.; Wilhelms-Dick, D.; Brey, T.; Abele, D., Coexistence of three calcium carbonate polymorphs in the shell of the Antarctic clam Laternula elliptica. *Geochemistry, Geophysics, Geosystems* **2012,** *13*, (5), Q05014.

39. Schindelin, J.; Arganda-Carreras, I.; Frise, E.; Kaynig, V.; Longair, M.; Pietzsch, T.; Preibisch, S.; Rueden, C.; Saalfeld, S.; Schmid, B., Fiji: an open-source platform for biological-image analysis. *Nature methods* **2012,** *9*, (7), 676.

40. Bolte, S.; Cordelieres, F. P., A guided tour into subcellular colocalization analysis in light microscopy. *Journal of microscopy* **2006,** *224*, (3), 213-232.

41. Palabos Parallel lattice Boltzmann solver. www.palabos.org

42. Chou, L. E. I.; Garrels, R. M.; Wollast, R., Comparative study of the kinetics and mechanisms of dissolution of carbonate minerals. *Chemical geology* **1989,** *78*, (3-4), 269-282.

43. Davison, S. M.; Yoon, H.; Martinez, M. J., Pore scale analysis of the impact of mixing-induced reaction dependent viscosity variations. *Advances in water resources* **2012,** *38*, 70-80.

44. Herrera, P. A.; Cortínez, J. M.; Valocchi, A. J., Lagrangian scheme to model subgrid-scale mixing and spreading in heterogeneous porous media. *Water Resources Research* **2017,** *53*, (4), 3302-3318.

45. Rubin, Y.; Sun, A.; Maxwell, R.; Bellin, A., The concept of block-effective macrodispersivity and a unified approach for grid-scale-and plume-scale-dependent transport. *Journal of Fluid Mechanics* **1999,** *395*, 161-180.

46. Pokrovsky, O. S.; Golubev, S. V.; Schott, J.; Castillo, A., Calcite, dolomite and magnesite dissolution kinetics in aqueous solutions at acid to circumneutral pH, 25 to 150 C and 1 to 55 atm pCO2: New constraints on CO2 sequestration in sedimentary basins. *Chemical geology* **2009,** *265*, (1-2), 20-32.

List of Figures

Figure 1. (a-b) 2-D microscopic images of precipitates at 1 μm resolution in the micromodel during the precipitation phase (t=75 hr, top) and the dissolution phase (t=89 hr, bottom). Three different locations of multiple pores (upstream, midstream, and downstream) and five different single pore locations (*i*-*v*) are shown. The central line of the micromodel is shown with a dashed red line. See Figure S2 for high resolution images. (c) Change of precipitate patterns in multiple pores at selected times. See Figure S5 for high resolution images.

Figure 2. Change of precipitate area (A_{2D}) and reactive surface area (*RSA*) over time in three multiple pore regions.

Figure 3. Change of precipitate patterns in single pores at five different locations (*i*-*v*). Locations are shown in Figure 1 and images were taken at 0.20 μm/pixel.

Figure 4. Comparison of the precipitate area (A_{2D}) and the reactive surface area (*RSA*) in the first pore (location *a*) at four different resolutions (0.2, 0.63, 0.31, and 1 μm per pixel) during the precipitation phase (t=55hr) and dissolution phase (t=94 hr). All estimates are normalized to the estimated areas using 0.2 μm resolution images. Results at 1μm resolution within a circle were estimated with the interpolated images at 0.2 μm resolution from 1 μm resolution images using bicubic interpolation. Figure S9 for high resolution images.

Figure 5. (a) An experimental image of precipitate distribution at 24 hr during the dissolution phase and (b-f) simulation results of the distribution of pH, flow velocity field, and super-saturation ratio (SR) with respect to calcite.

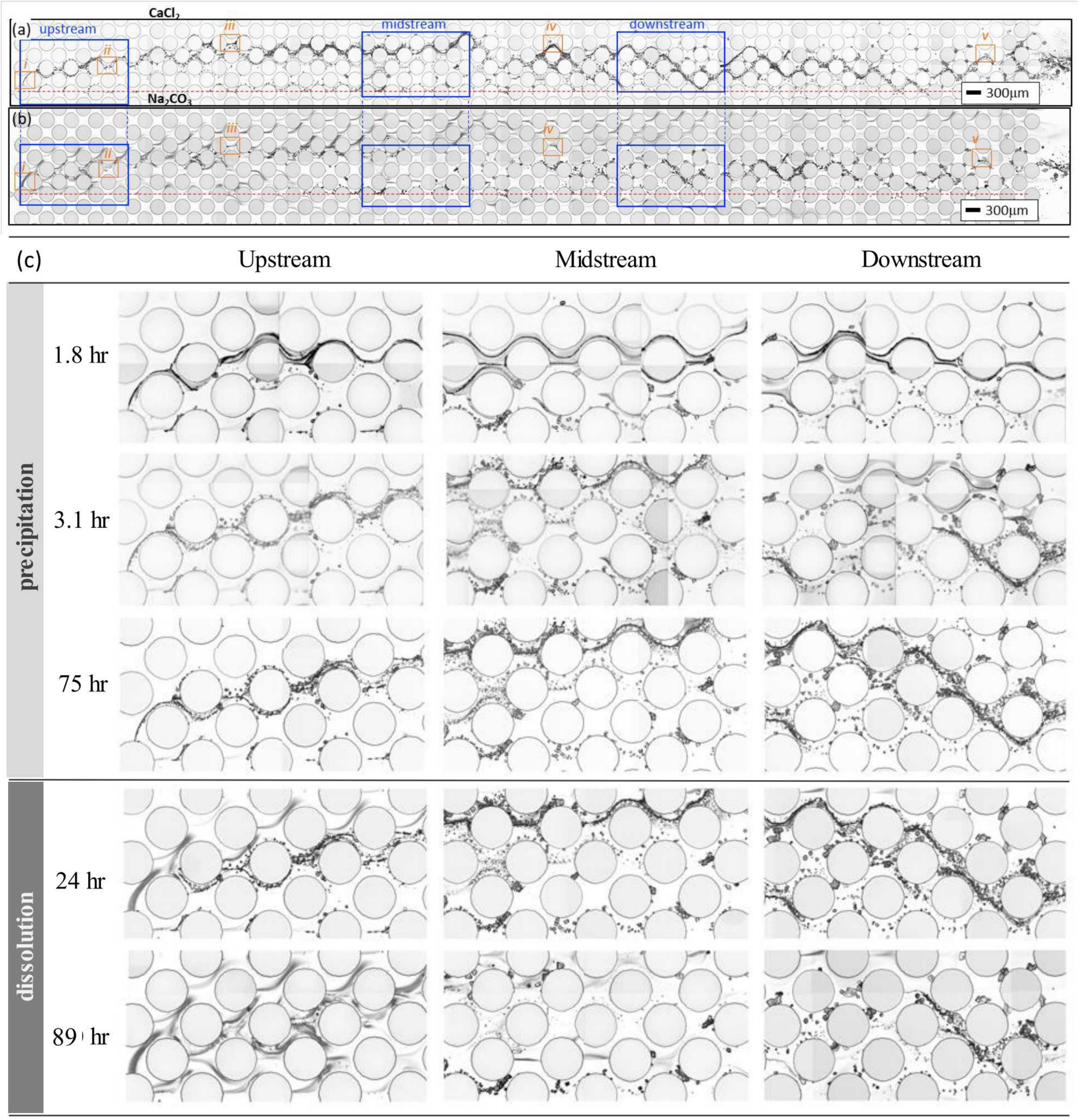

Figure 1. (a-b) 2-D micorscopic images of precipitates at 1 μm resolution in the micromodel during the precipitation phase (t=75 hr, top) and the dissolution phase (t=89 hr, bottom). Three different locations of multiple pores (upstream, midstream, and downstream) and five different single pore locations (*a*-*e*) are shown. The central line of the micromodel is shown with a dashed red line. See Figure S2 for high resolution images. (c) Change of precipitate patterns in multiple pores at selected times. See Figure S5 for high resolution images.

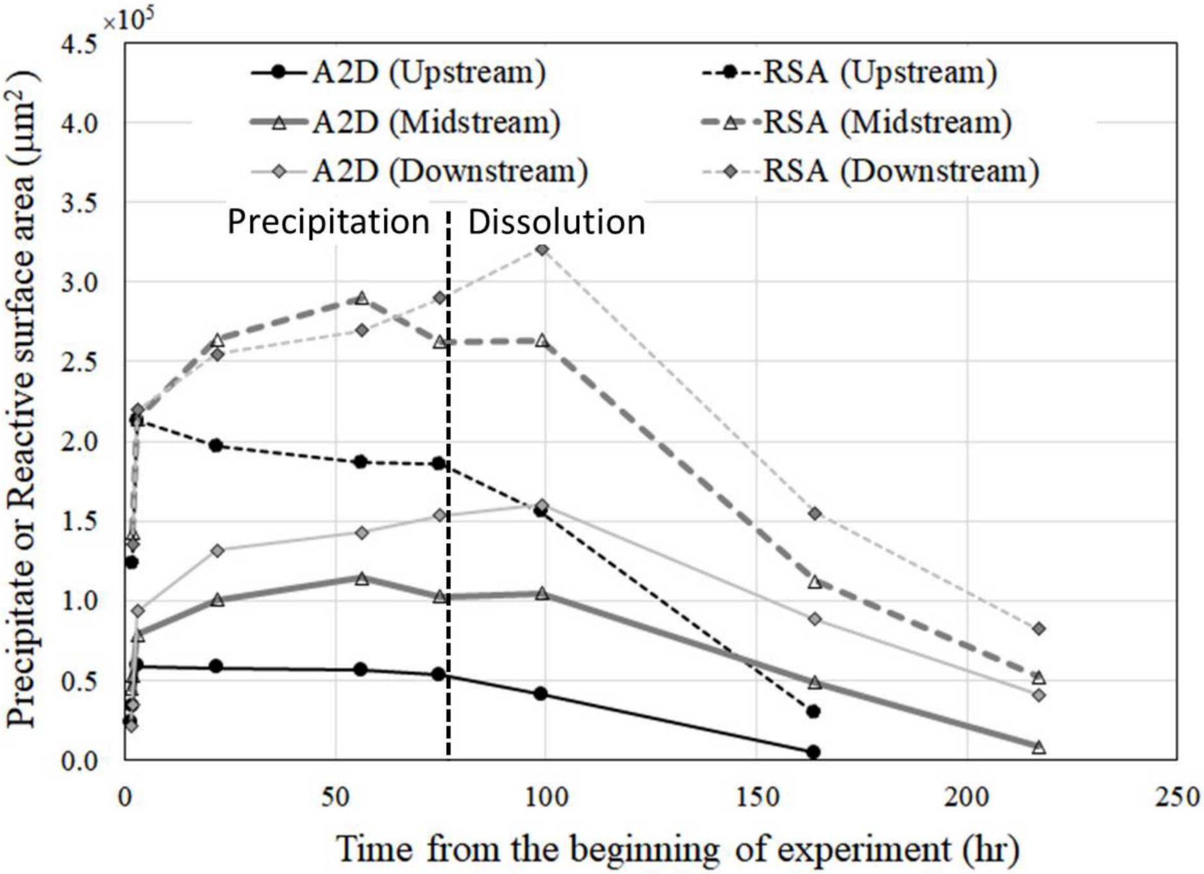

Figure 2. Change of precipitate area (A_{2D}) and reactive surface area (*RSA*) over time in three multiple pore regions.

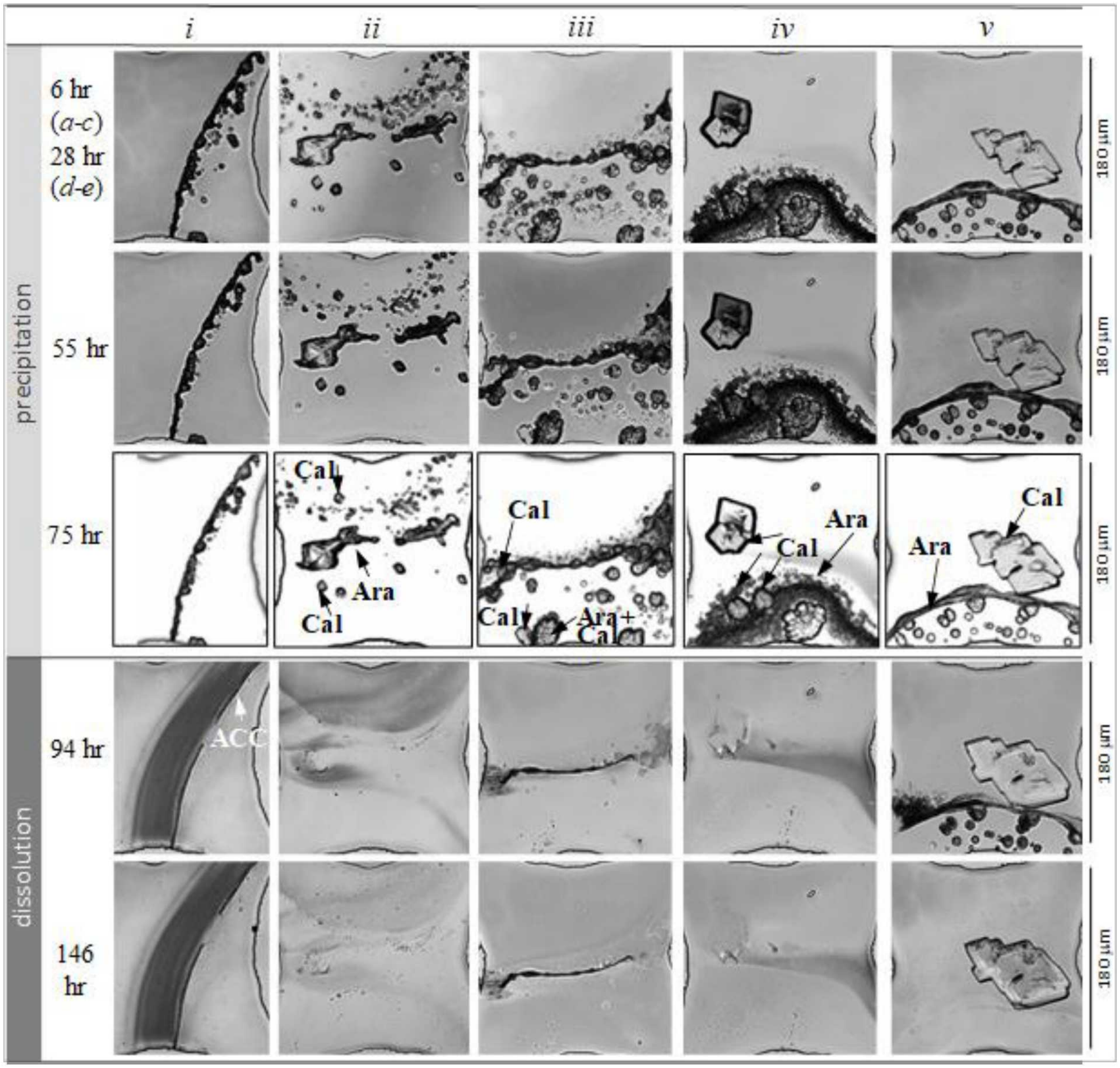

Figure 3. Change of precipitate patterns in single pores at five different locations (*i*-*v*). Locations are shown in Figure 1 and images were taken at 0.20 µm/pixel.

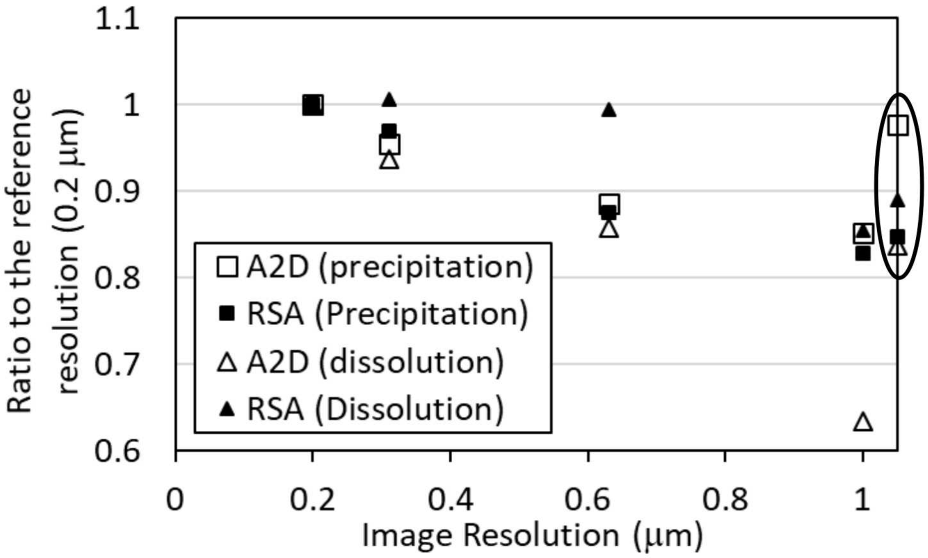

Figure 4. Comparison of the precipitate area (*A_{2D}*) and the reactive surface area (*RSA*) in the first pore (location *a*) at four different resolutions (0.2, 0.63, 0.31, and 1 µm per pixel) during the precipitation phase (t=55hr) and dissolution phase (t=94 hr). All estimates are normalized to the estimated areas using 0.2 µm resolution images. Results at 1µm resolution within a circle were estimated with the interpolated images at 0.2 µm resolution from 1 µm resolution images using bicubic interpolation. Figure S6 for high resolution images.

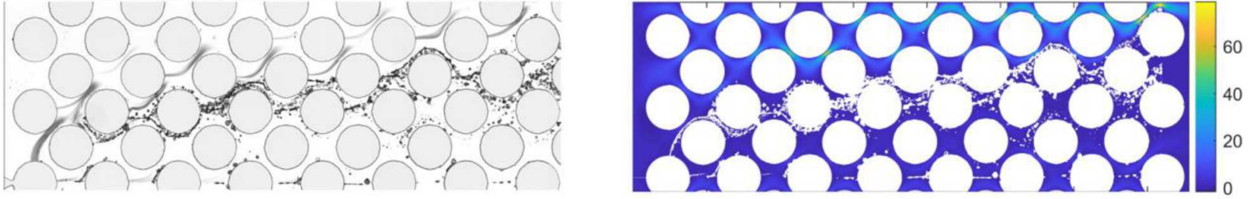

(a) Microscopy image at 24 hr during the dissolution phase

(b) Horizontal flow velocity (cm/min)

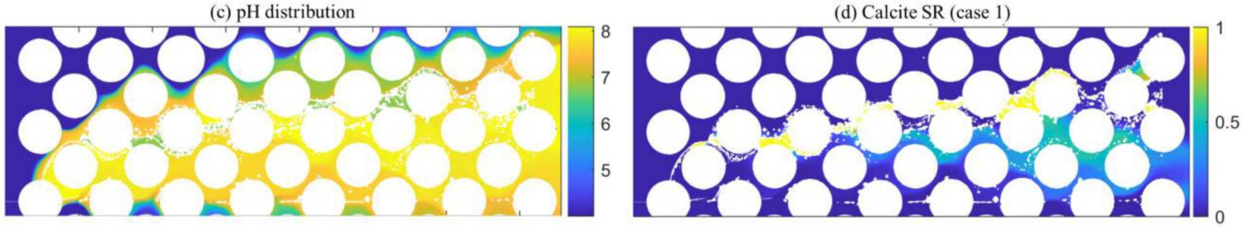

(c) pH distribution

(d) Calcite SR (case 1)

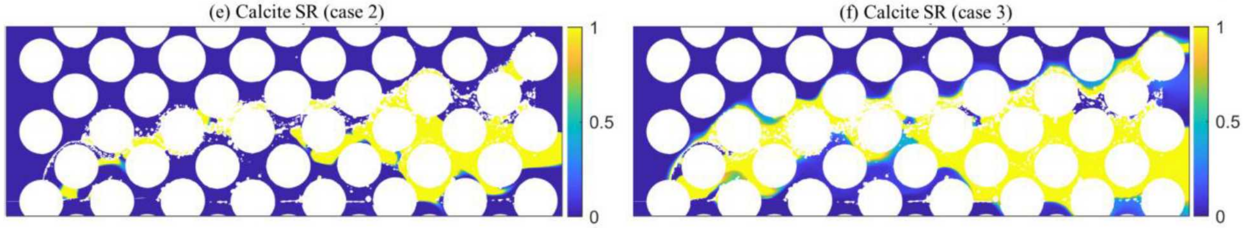

(e) Calcite SR (case 2)

(f) Calcite SR (case 3)

Figure 5. (a) An experimental image of precipitate distribution at 24 hr during the dissolution phase and (b-f) simulation results of the distribution of pH, flow velocity field, and super-saturation ratio (SR) with respect to calcite.

Table 1. Precipitate surface area (A_{2D}), overall reaction rate, reactive surface area (*RSA*), and effective reaction rate for multiple pore regions during precipitation (gray) and dissolution phases (white).

Time*	Overall reaction rate (mol/s)			Effective reaction rate (mol/m^2/s)		
(hr)	upstream	midstream	Downstream	upstream	midstream	downstream
1.5	1.2E-12	2.2E-12	1.1E-12	3.0E-05	2.8E-05	2.4E-05
1.8	2.6E-12	2.1E-12	3.3E-12	2.6E-05	1.4E-05	3.0E-05
3.1	1.5E-12	1.5E-12	3.4E-12	8.9E-06	8.5E-06	1.9E-05
22	-3.7E-15	8.8E-14	1.5E-13	-1.8E-08	3.7E-07	6.4E-07
56.2	-3.5E-15	3.0E-14	2.5E-14	-1.8E-08	1.1E-07	9.4E-08
75	-1.2E-14	-4.7E-14	4.3E-14	-6.5E-08	-1.7E-07	1.5E-07
99	-3.9E-14	7.7E-15	2.1E-14	-2.3E-07	2.9E-08	6.8E-08
164	-4.3E-14	-6.5E-14	-8.3E-14	-4.6E-07	-3.5E-07	-3.5E-07
217		-5.7E-14	-6.8E-14		-6.9E-07	-5.7E-07

* dt in Eq. (1) is the time interval of each image from the previous time step (i.e., the time difference between two images).

Supporting Information for

Pore-scale analysis of calcium carbonate precipitation and dissolution kinetics in a microfluidic device

Hongkyu Yoon[1,*], Kirsten N. Chojnicki[1], and Mario J. Martinez[2]

[1]Geoscience Research and Applications, Sandia National Laboratories, Albuquerque, NM, USA

[2]Fluid and Reactive Processes Department, Engineering Sciences, Sandia National Laboratories, Albuquerque, NM, USA

* Corresponding author (hyoon@sandia.gov)

The supporting information includes:

Section S1. Raman Spectroscopy

References

List of Supplementary Figures S1-S12

Figure S1. Schematic of micromodel with pore network dimension and inlet conditions

Figure S2. 2-D microscopic images of precipitates in the micromodel during (a) the precipitation phase (t=75 h) and (b) the dissolution phase (t=89 h). Three different locations of multiple pores (upstream, midstream, and downstream) and five different single pore locations (*i-v*) are shown. The central line of the micromodel is shown with a dashed red line. See Figure 1a-b for the description in the main text. High resolution image (1 μm resolution) is downloadable as a separate file.

Figure S3. High resolution 2-D microscopic images of precipitates in the micromodel during (a) the precipitation phase (t=75 h) and (b) the dissolution phase (t=89 h).

Figure S4. An example of image segmentation procedure.

Figure S5. High resolution images of change of precipitate patterns in multiple pores at selected times. The three different locations (upstream, midstream, and downstream) are shown in Figure 1a-b & Figure S2. High resolution image is downloadable as a separate file.

Figure S6. Comparison of precipitates at two different locations in the upstream region. The precipitates in the first two pores (location A) do not change notably (within 1-2 % difference) between 3.1 h and 22 h, but in location B small particles at 3.1 h in the upper pore body dissolved at 22 h. This happens during the precipitation phase because the precipitate line blocks the transverse mixing, resulting in undersaturated conditions in both upper and lower regions.

Figure S7. Comparison of precipitate sizes at the end of precipitation phase (t = 75 h) and during dissolution phase (t = 99 h) in the downstream region. Image is taken from the bottom part of the downstream region where the dissolved components transported from the upstream reprecipitate onto the existing precipitate particles. Note that there is one new small crystal formed at the bottom of the middle pore at t = 99h.

Figure S8. Raman spectra of the precipitates at different locations. Microscopic images of crystals are also shown. Amorphous calcium carbonate (upper left) does not have distinct peaks corresponding to the reference Raman spectra of other calcium carbonate polymorphs. Calcite and aragonite have been detected predominantly.

Figure S9. High resolution images of the precipitate area (A_{2D}) and the reactive surface area (*RSA*) in the first pore (location *i*) at four different resolutions (0.2, 0.63, 0.31, and 1 μm per pixel) during the precipitation phase (t=55h) and dissolution phase (t=94 h). See Figure 4 in the main text for discussion.

Figure S10. Comparison of 2-D image, average of 3-D segmented image stack, and 3-D profile of precipitates in location *i* during the precipitation phase (t =75h, top) and during the dissolution phase (t=94h, bottom). The 3-D profile is exaggerated vertically twice.

Figure S11. Individual image slice of 3D confocal image stacks on the surface of micromodel (left), at the center of depth (middle), and near the glass cover (right) in location *ii* at four different times.

Figure S12. Individual image slice of 3D confocal image stacks on the surface of micromodel (left), at the center of depth (middle), and near the glass cover (right) in location *v* at four different times.

Supplementary Table S1. Confocal imaging parameters at three different resolutions

Supplementary Table S2. Precipitate surface area (A_{2D}) and reactive surface area (*RSA*) in the multiple pores.

Other supporting information of high resolution images includes:

Figure S2-high resolution image.pptx

Figure S5-high resolution image.pptx

Section S1. Raman Spectroscopy

Following Boyd et al. (2014), backscattering Raman spectroscopy with the Horiba LabRAM HR Evolution confocal Raman system was used to characterize the polymorphs of $CaCO_3$ precipitates. Raman spectra were taken over a range of 0 and 1200 cm^{-1} using a 532 nm diode-pumped solid-state laser. Raman spectra of $CaCO_3$ polymorphs were obtained over a range of acquisition times from 10s to 30s to increase a signal to noise with adjusting a laser power level. Carbonate polymorphs were determined by comparing the Raman spectra to reference spectra from Nehrke et al. (2012). Briefly, calcite has the spectra peaks at 155, 282, 711, and 1085 cm^{-1}, aragonite at 155, 206, 705, and 1085 cm^{-1}, and vaterite at 105, 114, 267, 300, 740, 750, 1075, and 1090 cm^{-1}. The peaks at ~ 520 cm^{-1} and the shoulders at ~920 cm^{-1} correspond to the silicon surface of the micromodel. In the current experimental work, vaterite was not observed. But in our other similar testing, vaterite was observed near the inlet where precipitation occurred very rapidly. Raman spectra with microscopic images are presented in Figure SX. Since Raman spectra was measured as a point measurement, different $CaCO_3$ polymorphs within the micromodel was analyzed selectively. Hence, there is no quantitative analysis done over the entire period. However, it is possible to infer the polymorphs based on morphology and locations (i.e., different local chemical conditions) as in Boyd et al (2014).

References

Boyd, V.; Yoon, H.; Zhang, C.; Oostrom, M.; Hess, N.; Fouke, B.; Valocchi, A. J.; Werth, C., Influence of Mg2+ on CaCO3 precipitation during subsurface reactive transport in a homogeneous silicon-etched pore network. Geochimica et Cosmochimica Acta 2014, 135, 321-335.

Nehrke, G., Poigner, H., Wilhelms-Dick, D., Brey, T. and Abele, D., Coexistence of three calcium carbonate polymorphs in the shell of the Antarctic clam Laternula elliptica. Geochemistry, Geophysics, Geosystems 2012, 13(5), Q05014, doi:10.1029/2011GC003996.

Supplemental Figures

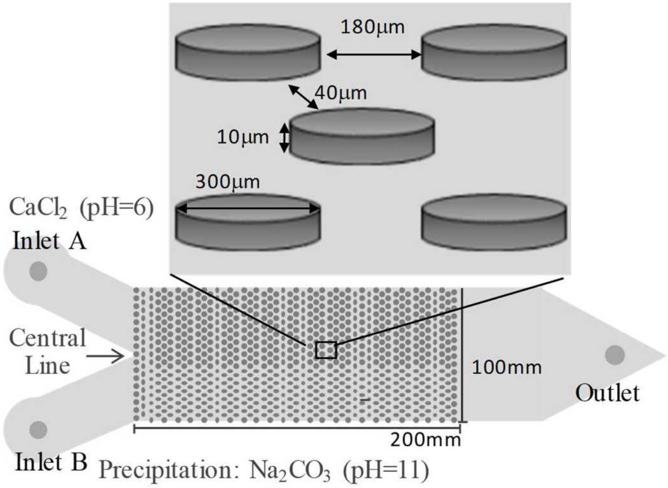

Figure S1. Schematic of micromodel with pore network dimension and inlet conditions

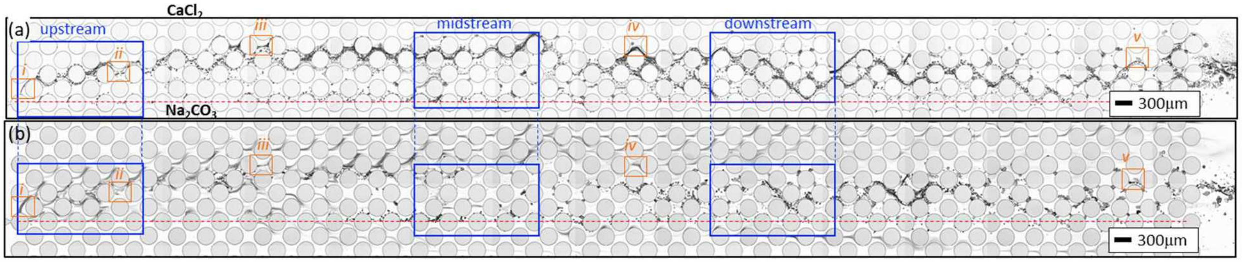

Figure S2. 2-D microscopic images of precipitates in the micromodel during (a) the precipitation phase (t=75 h) and (b) the dissolution phase (t=89 h). Three different locations of multiple pores (upstream, midstream, and downstream) and five different single pore locations (*i*-*v*) are shown. The central line of the micromodel is shown with a dashed red line. See Figure 1a-b for the description in the main text. High resolution image (1 μm resolution) is downloadable as a separate file.

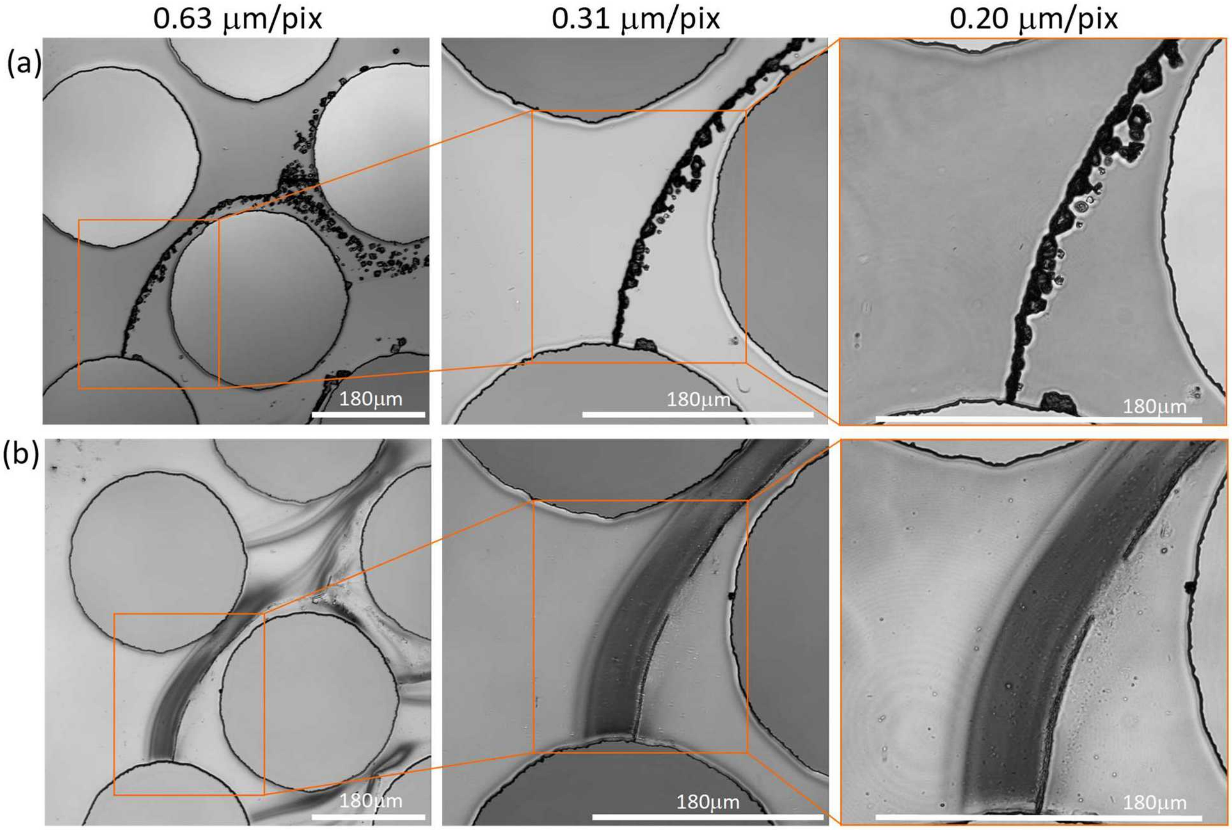

Figure S3. High resolution 2-D microscopic images of precipitates in the micromodel during (a) the precipitation phase (t=75 h) and (b) the dissolution phase (t=89 h).

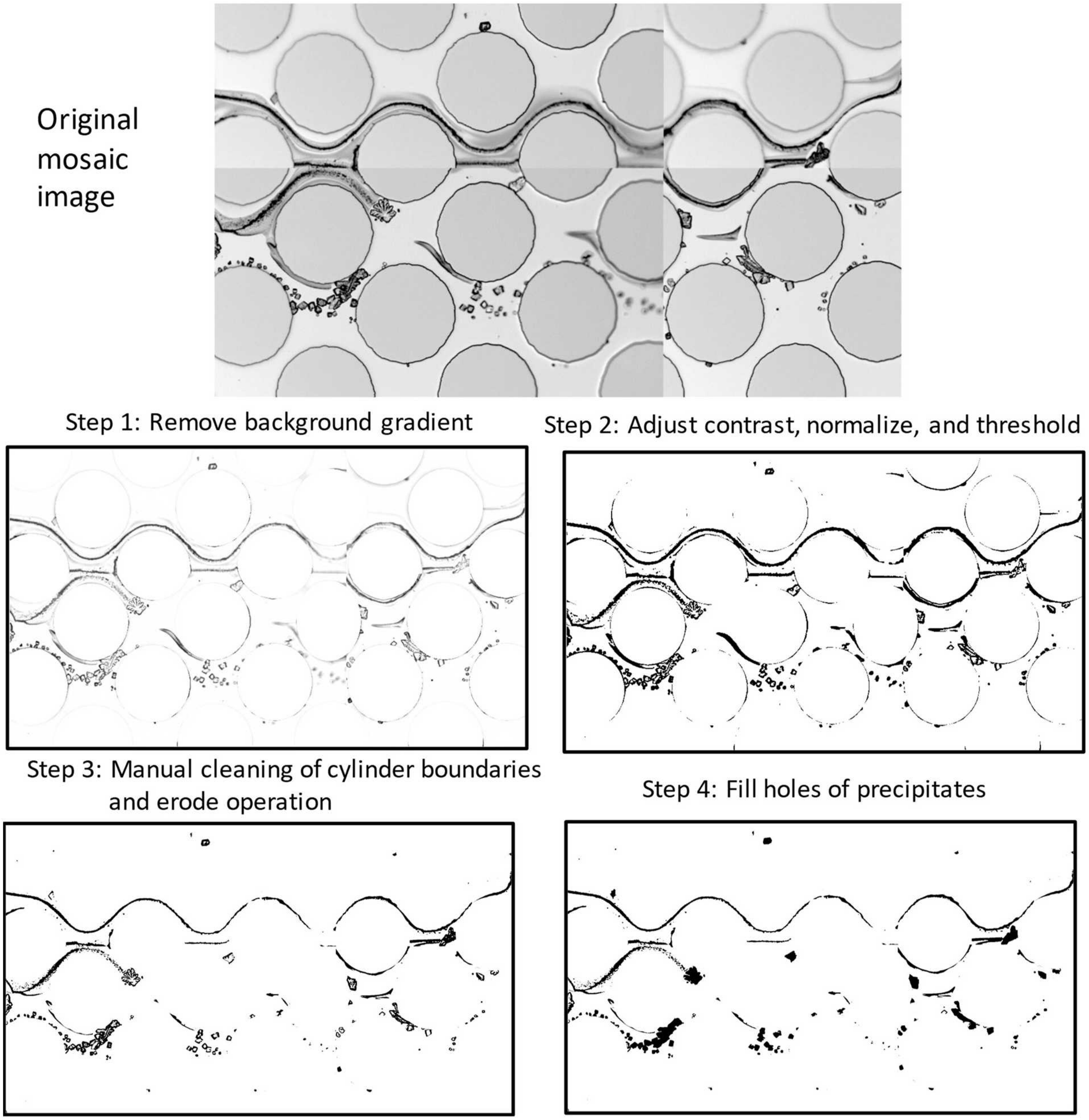

Original mosaic image

Step 1: Remove background gradient

Step 2: Adjust contrast, normalize, and threshold

Step 3: Manual cleaning of cylinder boundaries and erode operation

Step 4: Fill holes of precipitates

Figure S4. An example of image segmentation procedure.

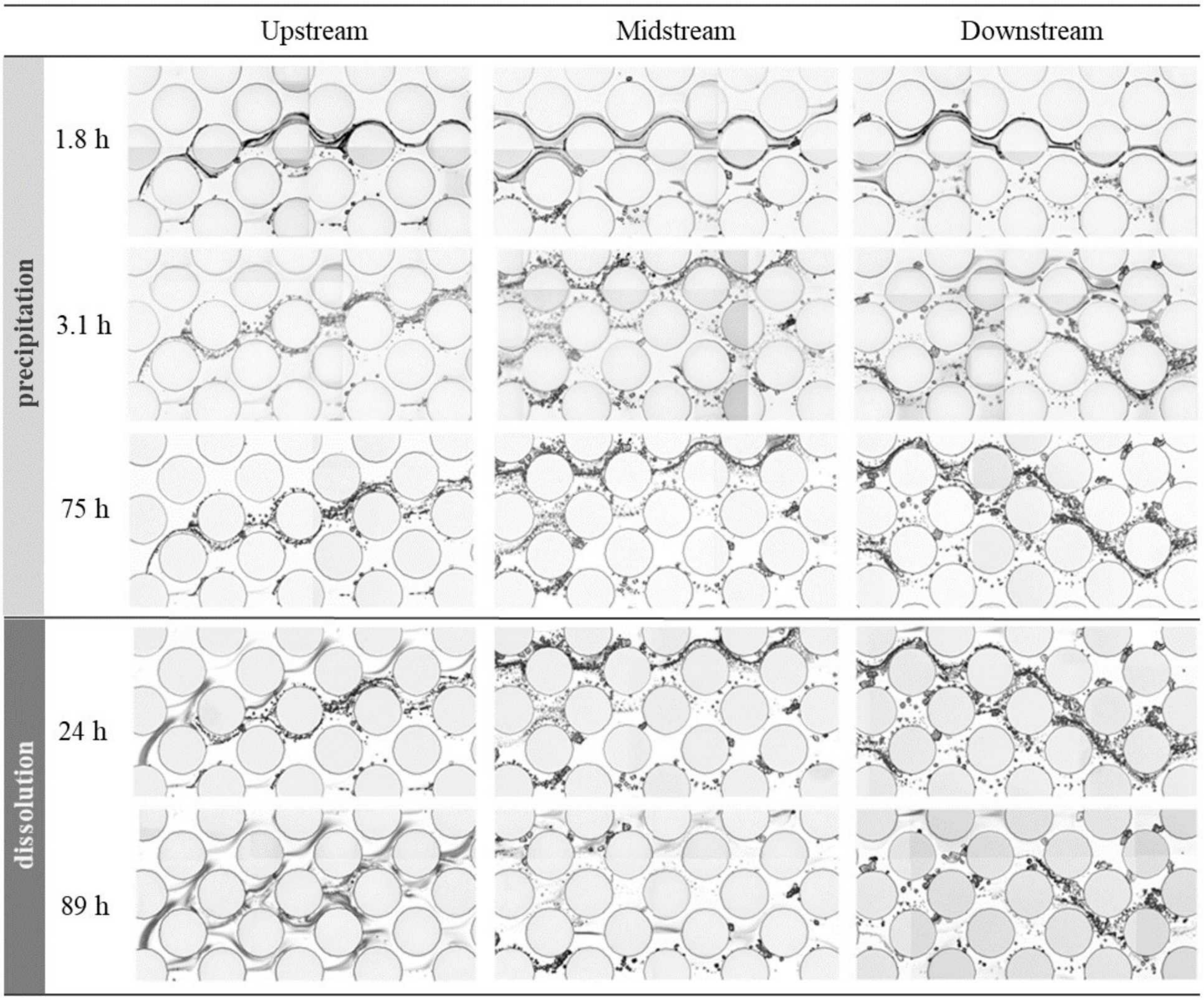

Figure S5. High resolution images of change of precipitate patterns in multiple pores at selected times. The three different locations (upstream, midstream, and downstream) are shown in Figure 1a-b & Figure S2. High resolution image is downloadable as a separate file.

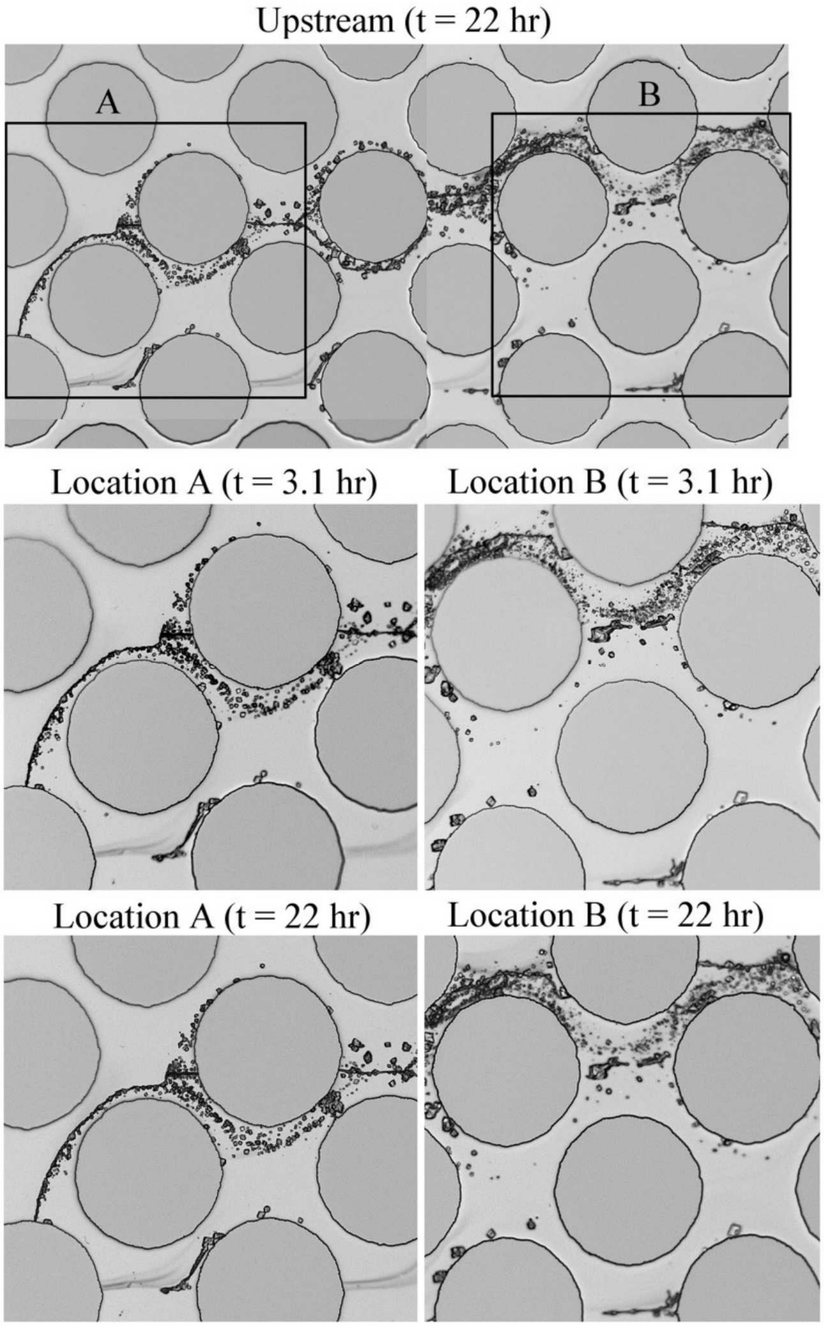
Upstream (t = 22 hr)

Location A (t = 3.1 hr)

Location B (t = 3.1 hr)

Location A (t = 22 hr)

Location B (t = 22 hr)

Figure S6. Comparison of precipitates at two different locations in the upstream region. The precipitates in the first two pores (location A) do not change notably (within 1-2 % difference) between 3.1 h and 22 h, but in location B small particles at 3.1 h in the upper pore body dissolved at 22 h. This happens during the precipitation phase because the precipitate line blocks the transverse mixing, resulting in undersaturated conditions in both upper and lower regions.

t = 75 hr (End of Precipitation phase)

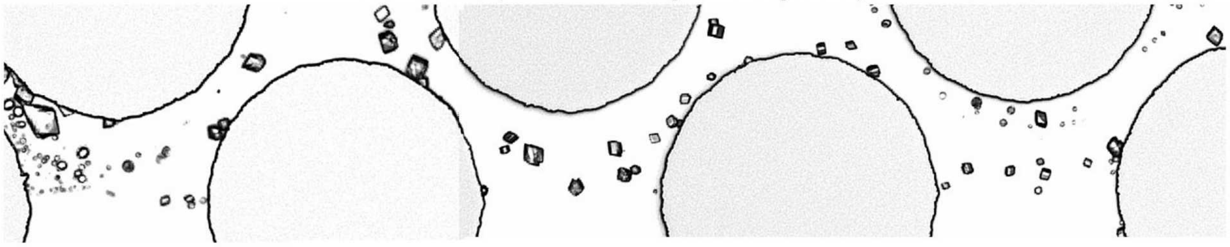

t = 99 hr (24 hr during dissolution phase)

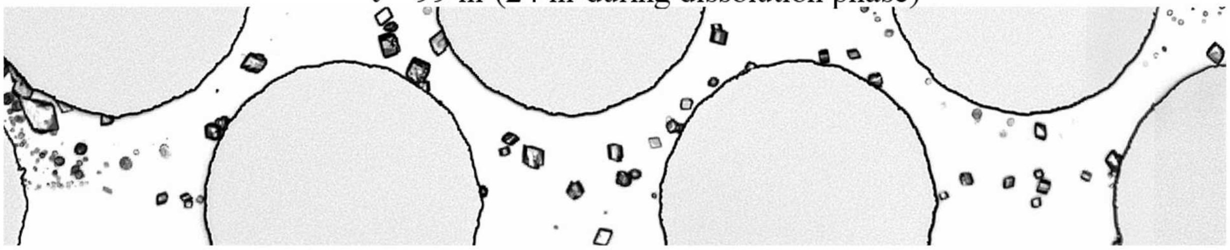

Figure S7. Comparison of precipitate sizes at the end of precipitation phase (t = 75 h) and during dissolution phase (t = 99 h) in the downstream region. Image is taken from the bottom part of the downstream region where the dissolved components transported from the upstream reprecipitate onto the existing precipitate particles. Note that there is one new small crystal formed at the bottom of the middle pore at t = 99h.

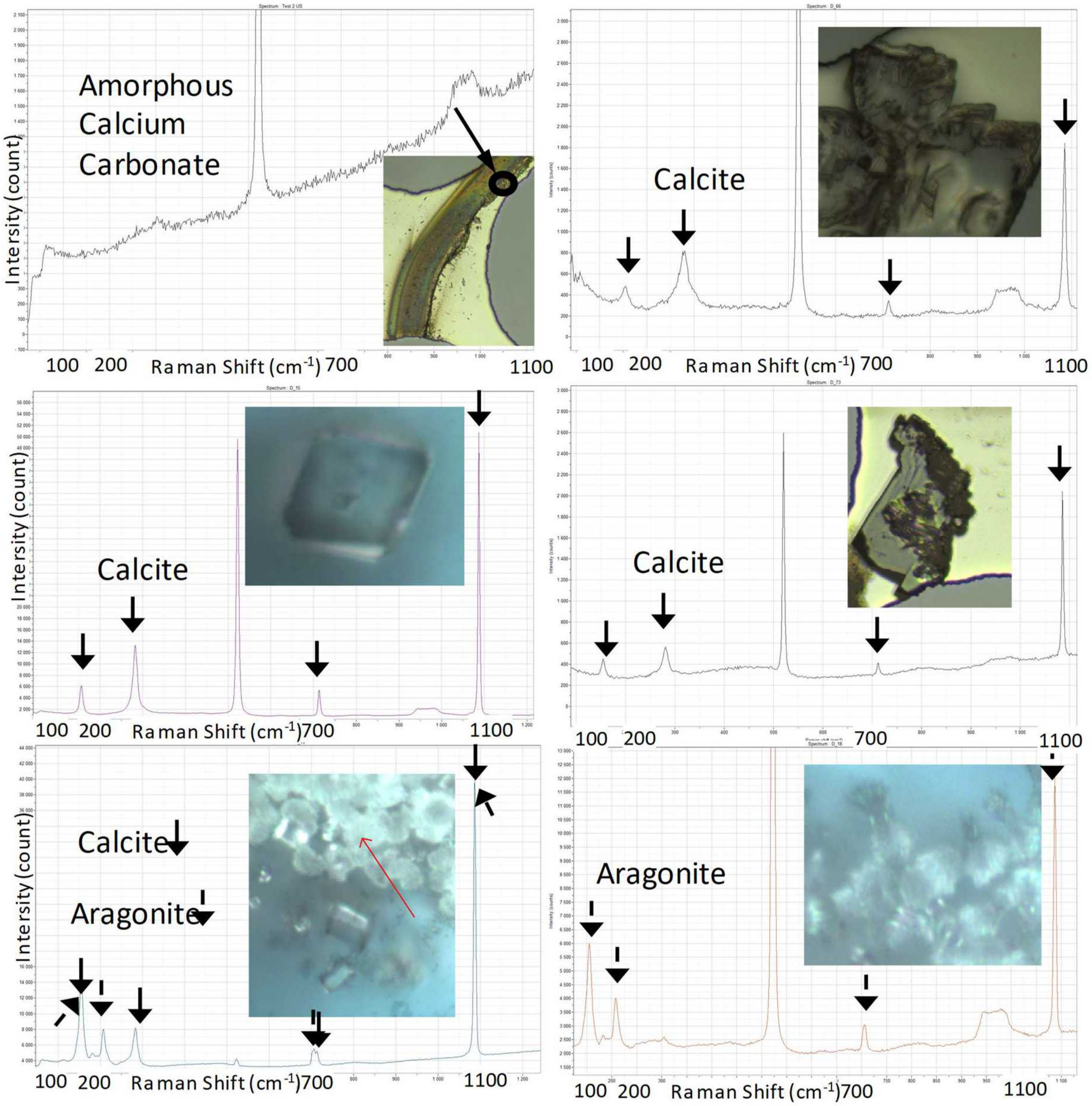

Figure S8. Raman spectra of the precipitates at different locations. Microscopic images of crystals are also shown. Amorphous calcium carbonate (upper left) does not have distinct peaks corresponding to the reference Raman spectra of other calcium carbonate polymorphs. Calcite and aragonite have been detected predominantly.

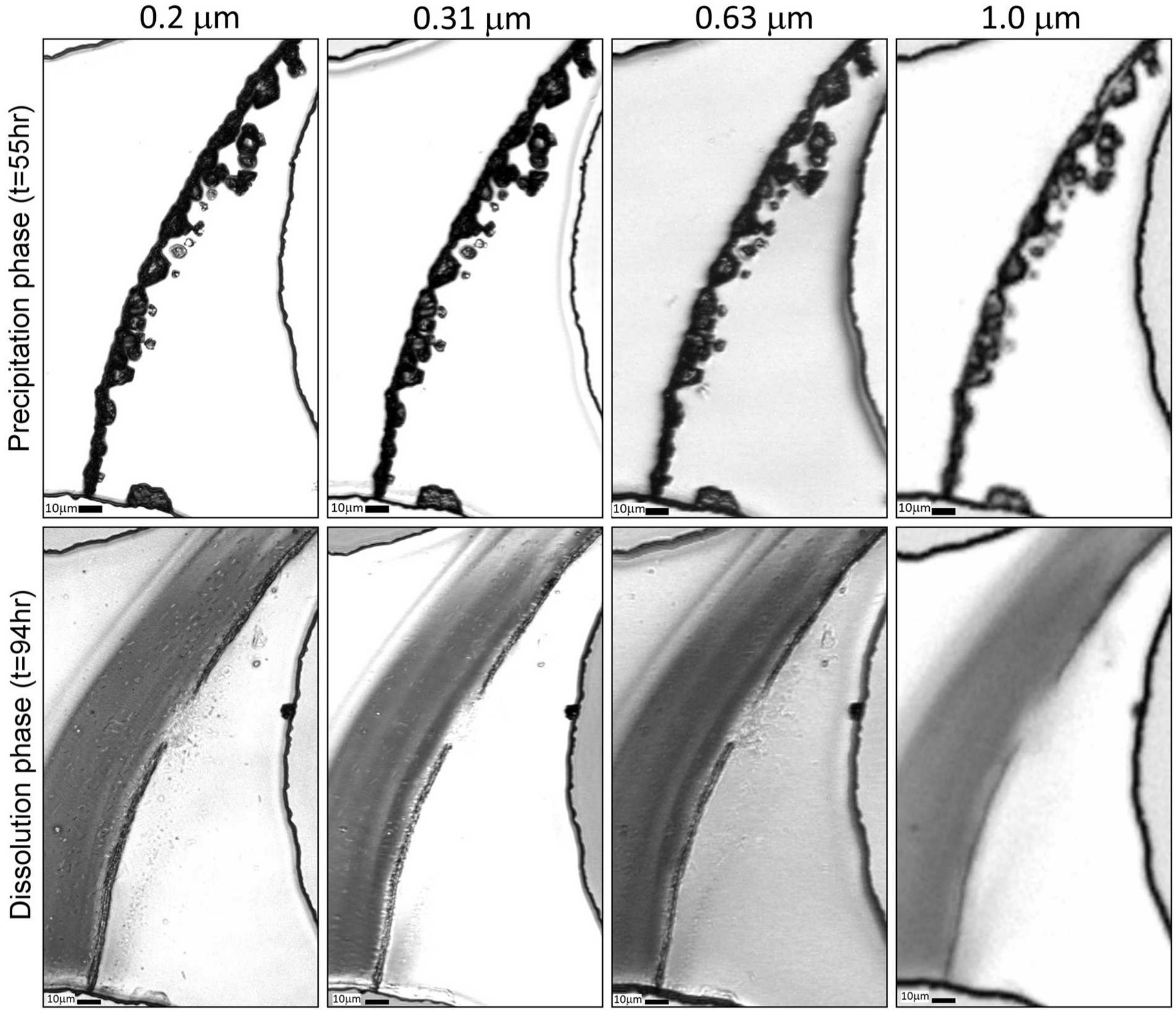

Figure S9. High resolution images of the precipitate area (A_{2D}) and the reactive surface area (*RSA*) in the first pore (location *i*) at four different resolutions (0.2, 0.63, 0.31, and 1 μm per pixel) during the precipitation phase (t=55h) and dissolution phase (t=94 h). See Figure 4 in the main text for discussion.

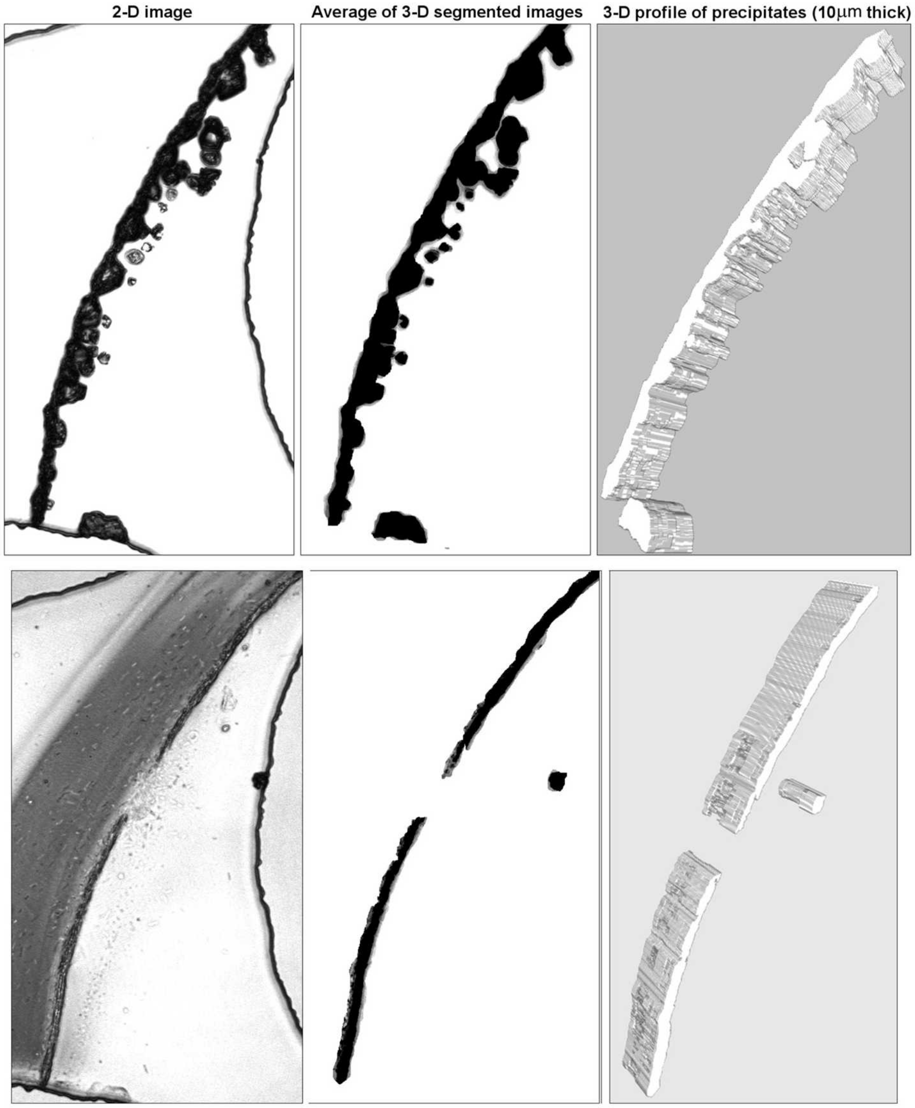

Figure S10. Comparison of 2-D image, average of 3-D segmented image stack, and 3-D profile of precipitates in location *i* during the precipitation phase (t =75h, top) and during the dissolution phase (t=94h, bottom). The 3-D profile is exaggerated vertically twice.

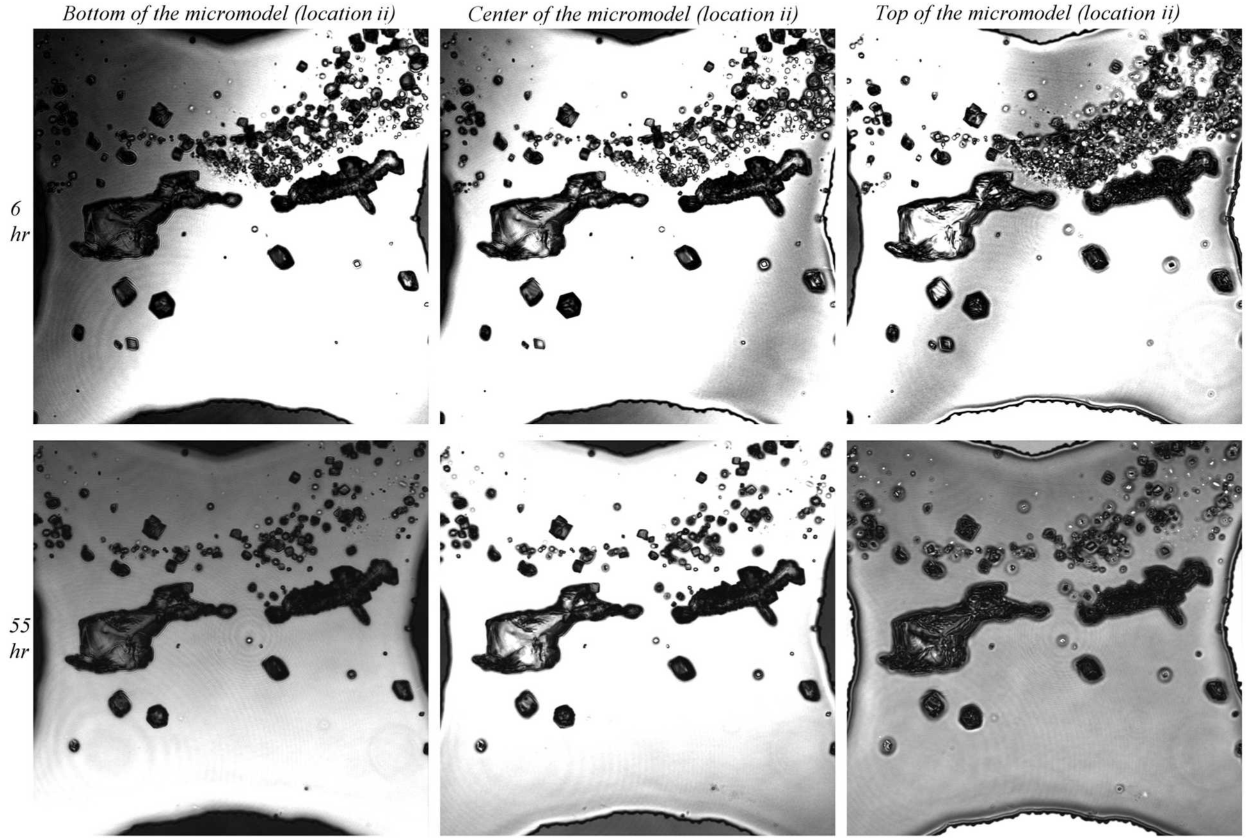

Figure S11. Individual image slice of 3D confocal image stacks on the surface of micromodel (left), at the center of depth (middle), and near the glass cover (right) in location *ii* at two different times.

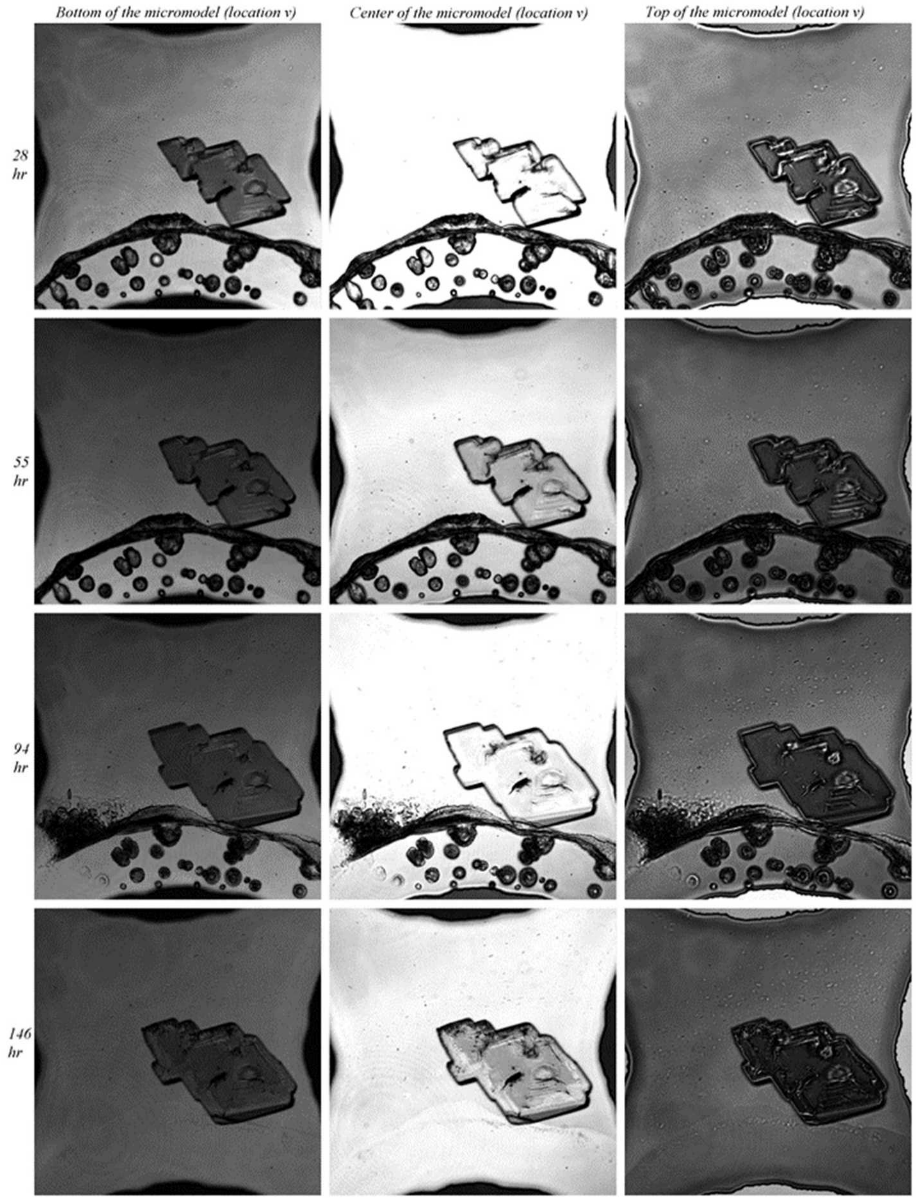

Figure S12. Individual image slice of 3D confocal image stacks on the surface of micromodel (left), at the center of depth (middle), and near the glass cover (right) in location *v* at four different times.

Table S1. Confocal imaging parameters at three different resolutions

x-y resolution (μm/pixel)	0.63	0.31	0.20
Image Size (microns)	642x642	321x321	200x200
Pinhole (AU)	0.40	0.68	0.15
Optical Thickness (μm)	7.5	4.9	1.9
Step Size (μm)	1	1	1
Objective	10x plan-neofluar	20x LD Epiplan	50x LD Epiplan-Neofluar
Numerical Aperature	0.3	0.4	0.55

Table S2. Precipitate surface area (A_{2D}) and reactive surface area (RSA)# in the multiple pores.

Time*	Precipitate area (μm^2)			Effective reaction rate (mol/m^2/s)		
(hr)	upstream	midstream	Downstream	upstream	midstream	Downstream
1.5	2.3E+04	4.4E+04	2.2E+04	7.8E+04	1.6E+05	8.9E+04
1.8	3.3E+04	5.3E+04	3.5E+04	1.2E+05	1.4E+05	1.4E+05
3.1	5.9E+04	7.8E+04	9.4E+04	2.1E+05	2.1E+05	2.2E+05
22	5.8E+04	1.0E+05	1.3E+05	2.0E+05	2.6E+05	2.5E+05
56.2	5.6E+04	1.1E+05	1.4E+05	1.9E+05	2.9E+05	2.7E+05
75	5.3E+04	1.0E+05	1.5E+05	1.9E+05	2.6E+05	2.9E+05
99	4.1E+04	1.0E+05	1.6E+05	1.6E+05	2.6E+05	3.2E+05
164	4.1E+03	4.9E+04	8.8E+04	2.9E+04	1.1E+05	1.5E+05
217		8.3E+03	4.1E+04		5.2E+04	8.2E+04

Overall reaction rates and effective reaction rates are reported in Table 1 in the main text.

* dt in Eq. (1) is the time interval of each image from the previous time step (i.e., the time difference between two images).